Journal of Hazardous Materials 416 (2021) 126158

Contents lists available at ScienceDirect

Journal of Hazardous Materials

journal homepage: www.elsevier.com/locate/jhazmat

Research Paper

Graphene oxide disrupted mitochondrial homeostasis through inducing intracellular redox deviation and autophagy-lysosomal network dysfunction in SH-SY5Y cells

Feng Xiaoli [a,b,1], Zhang Yaqing [c,1], Luo Ruhui [c], Lai Xuan [c], Chen Aijie [a], Zhang Yanli [a], Hu Chen [c], Chen Lili [d], Shao Longquan [a,b,*]

[a] Stomatology Hospital, Southern Medical University, Guangzhou 510515, China
[b] Guangdong Provincial Key Laboratory of Construction and Detection in Tissue Engineering, Guangzhou 510515, China
[c] Department of Stomatology, Nanfang Hospital, Southern Medical University, Guangzhou 510515, China
[d] Department of Stomatology, Union Hospital, Tongji Medical College, Huazhong University of Science and Technology, Wuhan 430022, China

ARTICLE INFO

Editor: Dr. S.Y. Chen

Keywords:
Graphene oxide
Mitochondrial stress
Redox deviation
Autophagy
Lysosomal alkalinization

ABSTRACT

Graphene oxide (GO) nanomaterials have significant advantages for drug delivery and electrode materials in neural science, however, their exposure risks to the central nervous system (CNS) and toxicity concerns are also increased. The current studies of GO-induced neurotoxicity remain still ambiguous, let alone the mechanism of how complicated GO chemistry affects its biological behavior with neural cells. In this study, we characterized the commercially available GO in detail and investigated its biological adverse effects using cultured SH-SY5Y cells. We found that ultrasonic processing in medium changed the oxidation status and surface reactivity on the planar surface of GO due to its hydration activity, causing lipid peroxidation and cell membrane damage. Subsequently, ROS-disrupted mitochondrial homeostasis, resulting from the activation of NOX2 signaling, was observed following GO internalization. The autophagy-lysosomal network was initiated as a defensive reaction to obliterate oxidative damaged mitochondria and foreign nanomaterials, which was ineffective due to reduced lysosomal degradation capacity. These sequential cellular responses exacerbated mitochondrial stress, leading to apoptotic cell death. These data highlight the importance of the structure-related activity of GO on its biological properties and provide an in-depth understanding of how GO-derived cellular redox signaling induces mitochondrion-related cascades that modulate cell functionality and survival.

1. Introduction

The rapid development of nanotechnology in various fields, ranging from engineering to electronics and biotechnology, has resulted in increasing applications of graphene-based nanomaterials (GBNs) (Yao et al., 2019). Compared with other graphene derivatives, graphene oxide (GO) possesses a larger specific surface area, affluent oxygen-containing groups, and more availability of surface functionalization, together making this material particularly attractive for biomedical applications (Atiroglu, 2020; Shen et al., 2020; Satapathy et al., 2020). However, the biomedical interest raised by GO nanomaterials (NMs) is two-fold. On one hand, GO can be used as tissue scaffolds that promote nerve regeneration, and as a strong candidate for replacing current intracranial or spinal devices due to its mechanical and electronic features (Chen et al., 2019; Niu et al., 2019; Liu et al., 2020). On the other hand, emerging in vitro and in vivo biosafety studies have revealed alarming findings (Gies and Zou, 2018; Xiaoli et al., 2020).

Among different hazard paradigms involved in biological behavior of NMs, such as formation of thrombus (Singh et al., 2012), inflammatory cell infiltration (Park et al., 2015), generation of oxidative stress (Russier et al., 2013), and DNA damage (Lu et al., 2017), the production of reactive oxygen species (ROS) is a major mechanism responsible for NM-induced cytotoxicity (Xiaoli et al., 2017; Zhang et al., 2020; Zhang et al., 2020). The intracellular ROS mainly comes from the electron leakage during mitochondrial aerobic respiration (Cadenas, 2018), however, in this study we detected that GO induced high levels of ROS

* Corresponding author at: Stomatology Hospital, Southern Medical University, Guangzhou 510515, China.
E-mail address: Shaolongquan@smu.edu.cn (S. Longquan).
[1] These authors contributed equally to this work.

https://doi.org/10.1016/j.jhazmat.2021.126158
Received 20 March 2021; Received in revised form 5 May 2021; Accepted 16 May 2021
Available online 24 May 2021

primarily through activation of the NADPH oxidase system located on the cytoplasm and plasma membrane. Studies on the antibacterial action of GO reported that the two-dimensional planar structure and surface functional groups of GO played crucial roles in ROS formation and its interaction with bacterial membranes (Liu et al., 2011; Li et al., 2016; Guo et al., 2017). Thus we wonder how the active chemical property of GO reacts to mammalian systems, particularly to the CNS, by mediating certain redox signaling. It's important to note that once there's an imbalance of redox in the cell, high levels of ROS will persistently attack lipids, proteins, DNA, and subcellular structures (such as the mitochondria and nucleus), leading to a series of cascades in living systems (Feng et al., 2015).

It is clear that several natural antioxidants in cells, such as glutathione, superoxide dismutase (SOD), and catalase, defend the cells against high concentrations of ROS. More importantly, autophagy acts as a defensive mechanism to limit ROS-triggered cell damage by removing oxidatively damaged molecules and organelles (Zhang et al., 2016; Li et al., 2020). Thus, the second paradigm in this paper lies in studying the disturbance in cellular autophagy levels following exposure to GO. At present, the elevated autophagy levels have been demonstrated to be involved in metal and metallic oxide NMs (Shen et al., 2019; Perez-Arizti et al., 2020; Simonet et al., 2020), it is not yet considered as an exact mechanism for GBN-related biological behavior. The dynamic process of autophagy is determined by autophagic flux, including autophagosome formation, the fusion between autophagosomes and lysosomes, and degradation within autolysosomes. Therefore, it is unclear if autophagy is actively induced or it is linked to excessive accumulation of autophagosomes resulting from impaired lysosomal degradation. Several metal oxide NMs (such as ZnO, CuO) have been reported to display pH-dependent solubility after internalization via endocytosis, suggesting the crucial role of acidic lysosomes in NM-induced cytotoxicity (Henson et al., 2019; Holmes et al., 2020). However, much remains unclear about the potential biodegradation of GBNs upon exposure to the non-conducive environment in cells (Soenen et al., 2015). What would be more interesting, is to investigate the influence of biodegradation property of GBNs on cellular redox signaling and further survival.

In the current study, we systematically explored the hydration activity of GO in a complete medium and demonstrated the underlying mechanism of its toxicity in human SH-SY5Y neuroblastoma cells. Currently permanently established neuronal cell models have been widely used to study neurological diseases to alleviate the challenge of culturing mature neurons. We choose SH-SY5Y cells as the research model for they are derived from human neuronal tumors and considered to be most reminiscent of catecholaminergic neurons and commonly used for toxicology evaluation (Kovalevich and Langford, 2013; Xicoy et al., 2017). Firstly, we identified the function of surface oxidized groups as well as free radicals in affecting the biological characteristics of GO. Next, we emphasized the contribution of ROS-initiated oxidative stress, followed by disturbances in the autophagy-lysosomal network, all leading to significant mitochondrial stress and consequently cell apoptosis. These data highlight the importance of the structure-related activity of GO on its biological behaviors and provide an in-depth understanding of how one biological parameter (GO-derived cellular redox signaling) can induce a cascade of effects that modulates nerve cell functionality and survival.

2. Materials and methods

2.1. Materials, reagents, and antibodies

Graphene oxide (GO) nanosheets were obtained commercially from Sigma-Aldrich (St. Louis, MO, USA). The chemical reagents N-acetyl-L-cysteine (NAC), rapamycin (RAPA), and GSK2795039 were purchased from MedChemExpress (MCE, China). 8-CPT-cAMP was purchased from Abcam (USA). Bafilomycin A_1 (Baf A_1), 3-methyladenine (3-MA), 3-IBMX, and forskolin were purchased from Topscience (Shanghai, China). FITC-BSA was purchased from Bioss Inc. (Beijing, China). TRITC-labeled phalloidin and RIPA lysate buffer were purchased from Solarbio (Beijing, China). BODIPY 581/591 C11 was purchased from Thermo Fisher (USA). MitoSOX Red indicator and LysoSensor™ Green DND-189 were purchased from Yeasen (Shanghai, China). DAPI was purchased from Beyotime (Shanghai, China). Earle's balanced salt solution (EBSS) was purchased from Gibco (USA). Anti-lysosome-associated membrane protein-1 (LAMP-1) antibody was purchased from Santa Cruz Biotechnology (USA). Antibodies against LC3I/II, Atg5, and Beclin1, p62/SQSTM1, and horseradish peroxidase (HRP)-conjugated secondary antibody were purchased from Cell Signaling Technology (USA). Anti-AMPK, anti-pAMPK, anti-ULK1, anti-pULK1, anti-mTORC1, anti-pmTORC1, anti-$p47^{phox}$, anti-$p67^{phox}$, anti-Bax, anti-cytochrome C (CytC), anti-COXIV, anti-Caspase 3, anti-cleaved Caspase 3, anti-Caspase 9, and anti-cleaved Caspase 9 antibodies were purchased from Proteintech (USA). Anti-NOX1, anti-NOX2, and anti-NOX4 antibodies were purchased from ABclonal (Wuhan, China). Anti-p-$p47^{phox}$ and anti-Na^+/K^+-ATPase antibodies were purchased from Abbkine (Wuhan, China). Anti-p-$p67^{phox}$ antibody was purchased from Affinity (USA).

2.2. Characterization of GO

The microstructure of GO samples was analyzed using scanning electron microscopy (SEM; Hitachi Scientific Instruments, Japan) and atomic force microscopy (AFM; Agilent Technologies, Inc., USA). To assess the hydration activity, 100 μg/mL GO nanosheets were dispersed in complete medium and sonicated for 1 h (50 W) in an ultrasonic processor (Biosafer, China). After incubation for 6 h and 24 h, the GO pellets were collected by centrifugation, and salts and organic compounds were removed by washing with 2.7 M hydrochloric acid and ethanol (Liu et al., 2015). The final products were washed with deionized water and freeze-dried for XPS analysis. The Raman spectroscopy (Renishaw, UK) was used to measure the molecular structure of GO samples with a laser excitation (50 mW) of 785 nm. The reactions between GO nanosheets and free radicals were studied on an electron paramagnetic resonance (EPR) spectrometer (Bruker, Germany) with 9.7858 GHz frequency and 3480G center field. 2,6,6-Tetramethyl-1-piperidinyloxy (TMPO) was used as an unpaired electron probe. The images of GO suspensions at different time points were captured. Finally, the zeta potential and hydrodynamic size of GO suspension (100 μg/mL) were evaluated respectively in culture medium and pure water using the Malvern Zetasizer Nano-ZS (Malvern Instruments Ltd., UK).

2.3. Abiotic pro-oxidative assays of GO

The pro-oxidative capacity of GO nanosheets (100 μg/mL) was assessed using specific chemical probes that selectively reacted with singlet oxygen ($^1O_2$) (BestBio, Beijing, China), superoxide anions ($O_2^{\cdot-}$) (Nanjing Jiancheng, Nanjing, China) under abiotic conditions. First, GO nanosheets were dispersed in complete medium and sonicated for 30 min, followed by incubation at 37 °C for 1, 3, 6, or 24 h. At indicated time points, the supernatant was collected by filtration using 0.22 μm membrane filters to remove additional materials, which otherwise would interfere with luminescence detection. The complete medium without GO treatment was selected as the control group. The prepared samples were subjected to pro-oxidative assays according to the manufacturer's instructions. Finally, a GSH consumption test in GO samples was performed using the GSH-Glo™ Glutathione Assay (Promega, USA) and detected on a BMG microplate reader (SPECTROstar Omega, Germany).

2.4. Cell culture and viability assessment

Human SH-SY5Y neuroblastoma cell line was acquired from the

Shanghai Cell Bank of Type Culture Collection of the Chinese Academy of Sciences. Cells were cultured in Dulbecco's modified Eagle's medium (DMEM) containing 10% fetal bovine serum (FBS) (Thermo Fisher, USA) and 100 IU penicillin and 100 mg/mL streptomycin (Gibco, USA) at 37 °C.

Before administration to cells, GO solutions were freshly prepared in complete medium and dispersed by sonication at 50 W for 30 min. SH-SY5Y cells were plated in a 96-well plate (NEST, Wuxi, China) at a density of 6×10^3/well. Next, the cells were treated with GO solutions with gradient concentrations of 5, 10, 20, 40, 60, 80, and 100 μg/mL. The control group was treated with the culture medium. After incubation for 3, 6, and 24 h, cell viability was assessed using the Cell Counting Kit-8 (CCK-8) assay (Dojindo Molecular Technologies, Japan) or the AlamarBlue assay (BestBio, Beijing, China) according to the manufacturer's instructions. To prevent the interference of GO materials with luminescence measurement, the supernatant from each well was transferred to an empty plate. Afterward, the absorbance was respectively measured at 490 nm or 560 nm by a microplate reader. To further investigate the death models of SH-SY5Y cells, cells were plated in 6-well plates and exposed to 40, 60, and 80 μg/mL GO for 24 h. NAC (600 μM) or a cAMP cocktail was added for stimulation in the rescue experiment. Next, cells were collected using EDTA-free trypsin and processed with a Annexin V-FITC/PI apoptosis kit (KeyGEN, Guangzhou, China). The cells were immediately subjected to flow cytometry (BD FACSAria III, NJ, USA) analysis.

2.5. Lysosomal reacidification

The cAMP cocktail, consisting of 8-CPT-cAMP (500 μM), forskolin (10 μM), and IBMX (100 μM) was used for lysosomal reacidification, as reported in previous studies (Coffey et al., 2014; Zhao et al., 2019).

2.6. Microscopy

Cellular morphology was observed under a 4KX41 phase-contrast microscope (Olympus, Japan). To further investigate the interactions between the surface membrane and GO materials, cells were seeded in 12-well plates with sterilized glass coverslips and treated with 40, 60 and 80 μg/mL GO for 24 h. Next, cells were washed with phosphate-buffered saline (PBS) and fixed in 4% paraformaldehyde (PFA) for 30 min. Afterwards, coverslips were dehydrated via gradient concentrations of ethanol, then embedded and observed using an S-3400N SEM (Hitachi Scientific Instruments, Japan). For TEM detection, 2.0×10^5 cells were grown in 6-well plates and subjected to 60 μg/mL GO with/without a cAMP cocktail for 24 h. The cells were subsequently collected by centrifugation and fixed in 2.5% glutaraldehyde and embedded in Epon resin. Finally, ultrathin cell samples (70 nm) were detected with the H-7500 TEM (Hitachi, Tokyo, Japan).

2.7. Cellular uptake of FITC-BSA-conjugated GO

FITC-BSA-conjugated GO samples were prepared as described before (Xiaoli et al., 2017). First, GO suspensions (1.0 mg/mL) and FITC-BSA solution were mixed with equal mass ratio and incubated at 37 °C overnight in dark. FITC-labeled GO pellets were obtained via centrifugation at 16,000*g* for 30 min and re-suspended with complete medium for immediate administration. For confocal imaging, 60 μg/mL FITC-BSA-GO were administered to cells for different time points (1, 3, 6, 12, and 24 h), washed using PBS, and fixed in 4% PFA for 1 h. Cytoskeleton and cell nucleus were respectively stained with TRITC-labeled phalloidin (100 nM) and DAPI in dark for 1 h. Photography were performed using a FV10i confocal microscope (Olympus, Japan).

2.8. Detection of membrane lipid peroxidation

Cells were incubated with different doses of GO (40, 60, and 80 μg/mL) for 6 h and stained with BODIPY 581/591 C11 peroxidation probe (10 μM) for 20 min. Photography were performed using a confocal microscope with excitation/emission wavelengths of 581/591 nm and 488/510 nm, respectively, to observe the conversion between reduced and oxidized fluorescent activity.

2.9. Detection of cellular redox deviation

The production of ROS was analyzed by the cell-permeable DCFH-DA dye assay (Beyotime, Nanjing, China). Cells were grown in 6-well plates and treated with GO samples for 6 h. NAC (600 μM) and NOX2-specific inhibitor (GSK2795039, 25 μM) were respectively applied in the rescue experiment. Cells were then harvested through trypsinization and stained using 10 μM DCFH-DA at 37 °C for 30 min and subjected to flow cytometry. Other detecting indexes for oxidative stress, including superoxide dismutase (SOD), catalase (CAT) and malondialdehyde (MDA) were estimated using commercial assay kits (Nanjing Jiancheng, Nanjing, China) according to the manufacturer's instructions. Total soluble protein content was measured using Coomassie blue staining. The NADP/NADPH content was determined using a specific assay kit purchased from Abbkine (USA). We next detected the activities of enzymes of three typical mitochondrial respiratory chain complexes, namely Complex I, Complex III, and Complex IV using commercial kits purchased from Solarbio (Beijing, China). Finally, cells were fixed in 4% PFA, followed by permeation in 0.2% Triton X-100 and blocked in 5% BSA. Cells were incubated with anti-NOX2 antibody overnight at 4 °C and labeled with indicated secondary antibodies for another 1 h at room temperature. The confocal microscope was used to observe intracellular fluorescence.

2.10. Mitochondrial dysfunction assessment

The activity of mitochondrial permeability transition pore (mPTP) was studied using a commercial kit purchased from Beyotime (Shanghai, China). Briefly, cells were subjected to different doses of GO for 24 h. Next, cells were stained with calcein AM, fluorescence quenching agent $CoCl_2$ or positive treatment Ionomycin (0.5 μM), and observed under the confocal microscope. To measure the mitochondrial membrane potential (ΔΨm), GO-treated cells were stained with 500 μL of JC-1 working solution for 20 min at 37 °C and analyzed using flow cytometry. Mitochondrial ROS (mtROS), a by-product of respiration, serves as another major source for intracellular ROS production. Therefore, cells were incubated with MitoSOX Red indicator (5 μM) for detecting the mtROS content and observed under an automatic fluorescent microscope (BX63, Olympus, Japan). The red fluorescence intensity was quantified using flow cytometry.

2.11. Intracellular ATP/AMP determination

The total mass of intracellular ATP was assessed using a commercial kit purchased from Beyotime (Shanghai, China). Cells were exposed to GO samples with/without NAC (600 μM) treatment for 24 h and lysed in a specific lysis buffer. Afterwards, the supernatant was collected by centrifugation at 12,000*g* at 4 °C for 5 min. ATP working solution was added to the samples and fluorescence intensity was determined using a BMG microplate reader. Cellular AMP was collected using a commercial kit purchased from Solarbio (Beijing, China) according to the manufacturer's instructions. The high-performance liquid chromatography (HPLC, Nexera XR LC-40, SHIMADZU, Japan) was used to assess AMP content.

2.12. Autophagic lentiviral transfection and imaging

SH-SY5Y cells at a density of 30,000 cells/well were seeded in a 24-well plate and transfected with stubRFP-sensGFP-LC3 lentivirus (GeneChem, Shanghai, China) following the instructions of the manufacturer. Cells stably expressing RFP-GFP-LC3 were seeded into 12-well plates and exposed to 60 μg/mL GO for 6 or 24 h. RAPA (100 nM) was administered to cells as a positive control. Next, cells were fixed with 4% PFA and labeled with DAPI for 15 min. Intracellular LC3-positive puncta were detected by a confocal microscope and quantitative analysis of fluorescence intensities was performed using ImageJ.

2.13. Lysosomal dysfunction evaluation

First, the fusion between autophagosomes and lysosomes was studied by immunofluorescence. Briefly, cells were treated with 60 μg/mL GO or RAPA (100 nM) for 24 h, followed by staining with anti-LAMP1 and anti-LC3 antibodies and corresponding secondary antibodies. The intracellular fluorescence was observed under a confocal microscope and analyzed using ImageJ software. For lysosomal acidity assay, cells were stained with LysoSensor Green DND-189 (Yeasen, Shanghai, China) for 30 min at 37 °C. In the rescue experiment, a cAMP cocktail was used to reacidify lysosomes. Next, cells were washed with PBS and detected using a fluorescence microscopy and quantitatively evaluated via the flow cytometry. The activity of lysosomal hydrolase, including acid phosphatase (ACP) and cathepsin B, were respectively determined using specific kits purchased from Leagene (Beijing, China) and Cusabio (Wuhan, China) according to the manufacturers' instructions. Fluorescence intensity values were calculated using a BMG microplate reader.

2.14. Cellular protein extraction

Cells were treated with 40, 60, and 80 μg/mL GO suspensions for 6 h or 24 h. 3-MA (10 mM), Baf A_1 (200 nM), and NAC (600 μM) and the cAMP cocktail were applied for different stimulations. To induce autophagy, cells were incubated in EBSS (starvation medium) or GO samples for 24 h and subsequently exposed to 3-MA (10 mM) for different time points (0, 1, 2, and 4 h). Cells were lysed using RIPA lysis buffer containing a mixture of proteases and phosphatase inhibitors to obtain total proteins. In addition, plasma membrane proteins were isolated using a commercial kit (Invent, USA) following the instructions of the manufacturer. Briefly, collected cells were lysed with buffer A, then transferred to a filter cartridge for differential centrifugation to separate membrane proteins and other cellular components. Plasma membrane proteins were suspended in buffer B and collected after super centrifugation, and finally dissolved in the Minute™ denaturing protein solubilization reagent. Similarly, mitochondria were isolated using the ExKine™ Mitochondrion Extraction Kit using a reagent-based method. The mitochondrial pellet was lysed in RIPA buffer and cytosolic supernatant was collected for western blotting.

2.15. Western blotting

An equivalent quantity of protein samples was subjected to SDS-PAGE and separated proteins were transferred to a polyvinylidene difluoride (PVDF) membrane (Merck Millipore, USA). Membrane-bound proteins were blocked in 5% fat-free milk and washed thrice with Tris-buffered saline in 0.1% Tween (TBST). The blots were incubated with indicated primary antibodies followed by incubation with HRP-conjugated secondary antibodies. The immunoreactivity was detected with a chemiluminescence substrate (EMD Millipore, USA), and then determined on enhanced chemiluminescence (ECL) detection system (Tanon, China). ImageJ software was used to analyze the optical densities. GAPDH, Na^+/K^+-ATPase, and COX IV were used as loading controls for total protein, plasma membrane protein, and mitochondrial protein, respectively.

2.16. Statistical analysis

Data were obtained from at least three independent experiments. The statistical analysis was conducted using GraphPad Prism 5 (USA) using a two-sided unpaired Student's *t*-test or one-way analysis of variance (ANOVA). $p < 0.05$ was considered as statistically significant.

3. Results and discussion

3.1. Pro-oxidative capability was related to the structural activity of GO nanosheets

The physicochemical properties of graphene nanomaterials, such as size, oxidation states, and functional groups, greatly influence their biological behavior and properties. In this study, a type of commercially available GO nanosheet was used to determine its potential neurotoxicity. Moreover, it was thoroughly characterized before exposing the SH-SY5Y cell line to it. TEM images showed that GO samples consisted of nanosheets with sharp edges and a lateral size ranging from 300 to 800 nm (Fig. 1A). The average thickness of GO in AFM analysis was approximately 1.0 nm (Fig. 1B), suggesting the single-layered structure of GO nanosheets. Considering the use of GO in cellular studies, we next investigated their hydrodynamic size and zeta potential in pure water and culture medium (Table 1). Most of the GO samples demonstrated distinct agglomeration, resulting in varying hydrodynamic diameters of 741.50 ± 205.40 nm, 641.30 ± 74.47 nm, and 561.30 ± 115.60 nm in respective solutions. We found that the zeta potential of GO in pure water was –29.40 ± 5.10 mV, whose absolute value was considerably higher than that of materials in the medium, suggesting that GO was more stably dispersed in pure water. The culture medium contained several proteins and inorganic ions, which could be adsorbed onto the GO surface to form the protein crown and interfere with the aggregation effect of GO suspensions (Koh et al., 2016; Xiaoli et al., 2020). Under these considerations, we believe that GO nanosheets dispersed in the medium could aggregate to form a bulk material that easily precipitated from the solution, resulting in increased hydrodynamic diameter size of GO in pure water than in the medium. This phenomenon was further visualized by images of GO suspensions acquired at different incubation time points (Fig. 1I). After the incubation time was extended to 24 h, a large number of evenly dispersed GO materials settled to the bottom of the tube, and the color of the medium was clearer than that of 1, 3 and 6 h.

At present, ultrasonic processing is widely applied with or without the addition of organic dispersants to obtain a homogeneous dispersion of graphene materials (Maktedar et al., 2017; Pattammattel et al., 2017). However, this strong mechanical force could destroy the primary structure of nanomaterials, producing fragmentation and defects on the surface or edges, and affecting their behaviors in the biological system (Gies and Zou, 2018). In this study, Raman spectroscopy was used to detect the typical D and G bands representative of GO and to confirm minimal structural alterations (Fig. 1D). As shown in Table 2, the intensity ratio of D to G band (I_D/I_G ratio) increased from 1.408 to 1.657 (incubation for 6 h) and 1.652 (incubation for 24 h) in GO samples following 1 h ultrasonic dispersion. Considering that Raman I_D/I_G ratios are indicative of the level of graphene surface defects (including oxygen-containing surfaces and structural defects), we believed that more number of defects were produced on the surface of GO nanosheets. These defects could be sites for the production of ROS as reported in Zhao and Jafvert's (2015) study. XPS was used to evaluate the functional groups on the surface of GO. As demonstrated in Table 2, similar atomic percentages of total oxygen were found between pristine GO (31.81%) and ultrasound-processed GO following incubation for 6 h (30.43%). However, with an increase in the incubating time, the total oxygen content decreased to 26.88% in GO samples incubated in the medium for 24 h. It was reported that light irradiation would change the oxidation state of GO in the aqueous solution (Zhao and Jafvert, 2015) , thus we

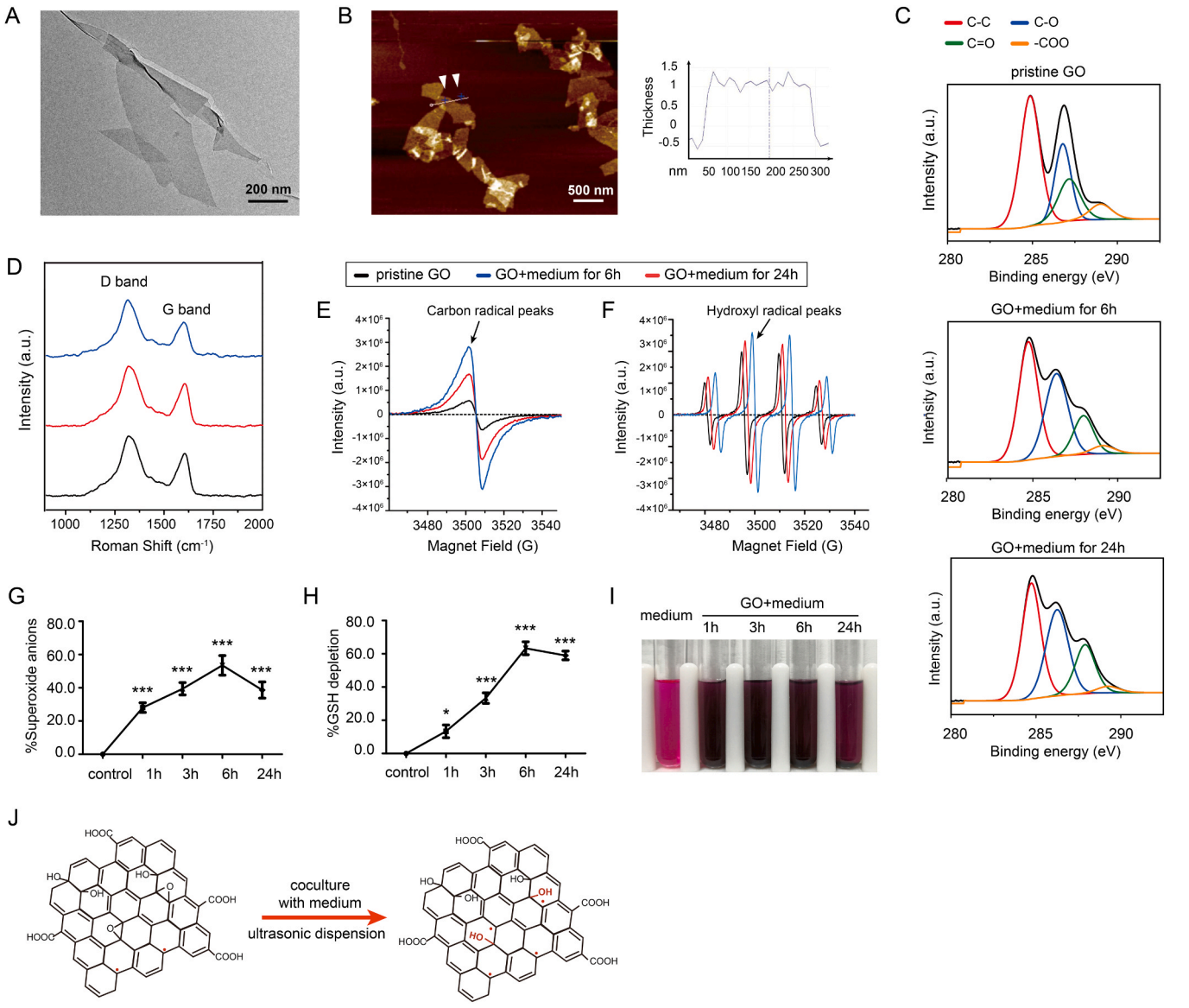

Fig. 1. Characterization and pro-oxidative capacity of GO nanosheets. (A) SEM image of GO morphology; (B) AFM image and thickness analysis of GO. The white line indicated by white triangles in the image represents the location of the thickness analysis; GO samples (100 μg/mL) were firstly dispersed in complete medium and sonicated for 1 h. After incubated for 6 h and 24 h, the GO pellets were collected via centrifugation followed by washing with hydrochloric acid and ethanol. The final products were washed with deionized water and subjected to XPS analysis (C), Raman spectrum identification (D), EPR assessment of the formation of carbon radicals (E) and hydroxyl radicals (F). Similarly, GO dispersions in medium were sonicated for 30 min and incubated at 37 °C for 1, 3, 6 and 24 h. At indicated time points, the supernatant was collected by filtration and subjected to superoxide anions assay (G) and abiotic glutathione assay (H). Additionally, the photographs of GO suspensions at different time points were displayed in (I); (J) Schematic describing the link to radical generation on GO surface following ultrasonic dispersion. Values are presented as mean ± S.D. from 3 independent measurements. * $P < 0.05$, *** $P < 0.001$ compared to the control group, respectively. For interpretation of the references to color in this figure legend, the reader is referred to the web version of this article.

Table 1
Zeta potential and hydrodynamic diameter of GO samples (n = 3).

GO samples	In pure water	In basal culture medium	In complete culture medium
Zeta potential (mV)	-29.40 ± 5.10	-8.20 ± 0.98	-7.24 ± 1.88
Hydrodynamic diameter (nm)	741.50 ± 205.40	641.30 ± 74.47	561.30 ± 115.60

Table 2
GO surface functional groups, radical density and defect levels.

GO samples	XPS (at%)				EPR (10^5) ·C	EPR (10^5) ·OH	Raman (I_D/I_G) Defects
	Total oxygen	C-OH	C=O	C-O-C			
GO	31.81	16.58	12.55	4.57	5.733	39.704	1.408
GO-6 h	30.43	25.33	10.3	2.42	28.123	51.850	1.657
GO-24 h	26.88	26.47	13.78	2	16.765	46.610	1.652

wonder more obvious decrease in total oxygen content (24 h) may be linked to longer incubation time in medium, especially under the condition that an increase in structural defects was detected on the GO surface. In contrast, the atomic percentages of oxygen functional groups changed to varying degrees as shown in XPS C1s spectra (Fig. 1C). Among these, the content of C-OH increased significantly from 16.58% to 26.47%, whereas that of C-O-C decreased from 4.57% to 2% (Table 2)

after incubation for 24 h. We further used EPR (Fig. 1E and F) to assess the effect of ultrasonic treatment on the generation of free radicals including carbon radicals (•C) and hydroxyl radicals (•OH). It could be found that both carbon radical peak (28.123×10^5) and hydroxyl radical peak (51.850×10^5) reached the highest in GO samples incubated in the medium for 6 h. These results suggested that epoxy rings could be opened through ultrasonic processing to react with nucleophiles in the culture medium, generating C-OH groups and free radicals (Fig. 1J), which exhibited a similar effect with hydration process as reported in Li et al. (2016, 2018) studies.

The presence of unpaired electrons of free radicals can react with molecular dioxygen to produce other types of ROS (Valko et al., 2016). Using selective and highly reactive chemical probes, we detected formation of O_2^- (Fig. 1G), but not $^1O_2$ (Fig. S1) in GO-exposed medium, which peaked following 6 h incubation. An abiotic GSH-Glo™ assay was further conducted to confirm the pro-oxidative capacity of GO materials. The GO suspensions were depleted of GSH resulting in maximum consumption by 61% at 6 h (Fig. 1H). Based on these findings, there exists a correlation between the surface radical density, the degree of pro-oxidant activity, and ultrasonic processing in the culture medium for GO nanosheets. A recent study reported that electrons from biological reducing agents could be transferred from single-walled carbon nanotubes to molecular oxygen, generating ROS, and damaging DNA (Hsieh et al., 2014). Therefore, we believe that a similar mechanism resulting in oxidative stress can occur in GO and responsible for its toxicological effects.

3.2. GO caused cytotoxicity in neuronal cells manifested as apoptotic cell death

First, the adverse effects of GO on cell proliferation were assessed using the CCK-8 assay. Based on the data in Fig. 2A, at concentrations of GO samples lower than 20 μg/mL, no change in cell viability was discovered despite increasing the incubation time to 24 h. On the contrary, the cell survival rate was significantly reduced (less than 66%) following 3 h treatment of GO at a concentration higher than 40 μg/mL. Furthermore, with the increase in the incubating time, 50% lethal dose (LD_{50}) of GO materials in SH-SY5Y cells decreased from 100 μg/mL to 60 μg/mL. Therefore, GO triggered dose and time-dependent toxicity to SH-SY5Y cells. To further investigate the link between GO-induced cytotoxicity and oxidative stress, cells were treated with a redox indicator, alamarBlue (Bonnier et al., 2015). Cells in a proliferative state are in a reductive environment, thus internalized alamarBlue may be reduced and then released into the culture medium, emitting pink fluorescence. When the cell proliferation is stronger, its fluorescence is brighter. Fig. 2B reveals a decline in cell survival rates, suggesting an

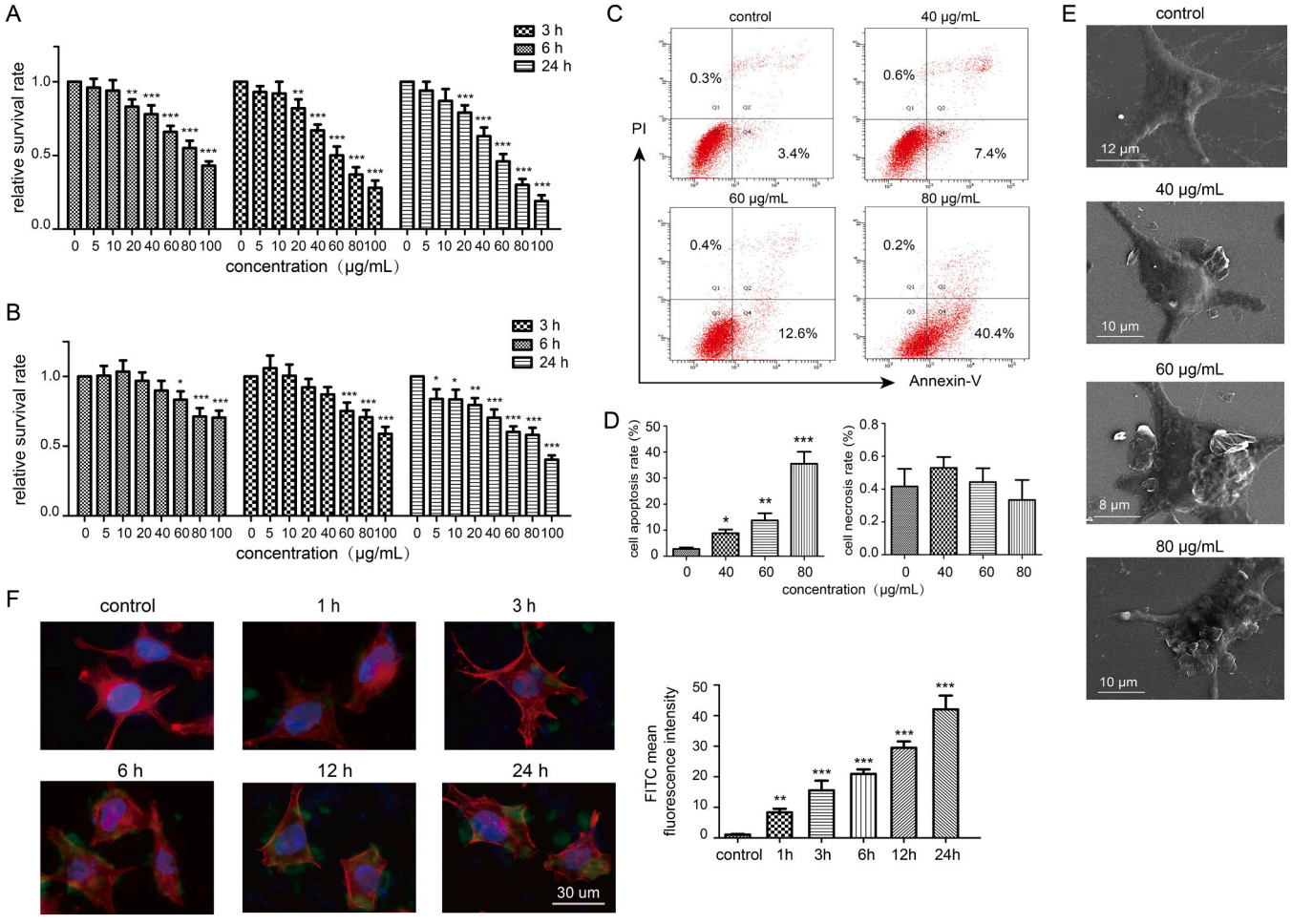

Fig. 2. Cellular uptake and cytotoxicity of GO exposed to SH-SY5Y cells. Cells were exposed to GO suspensions of 5, 10, 20, 40, 60, 80 and 100 μg/mL for different times points (3, 6 and 24 h) and subjected to CCK-8 assay (A) and alamarBlue assay (B) for cell viability. (C) Cells were treated with 40, 60 and 80 μg/mL GO for 24 h and stained with the Annexin V-FITC/PI dye for 30 min, and collected for flow cytometer analysis. Quantitative analysis of cell apoptosis rate and necrosis rate were displayed in the below histogram (D). (E) SEM image of GO treated cells following 24 h incubation. (F) Cells were incubated with 60 μg/mL FITC-BSA-GO for different time points (1, 3, 6, 12 and 24 h) and fixed in 4% PFA for 1 h. Cytoskeleton and nuclei were respectively stained with TRITC labeled phalloidin (100 nM) and DAPI. Representative images were captured using a confocal microscope and intracellular FITC fluorescence intensities were quantified in the right histogram. All quantitative data are presented as mean ± SD of 3 independent tests, * $P < 0.05$, ** $P < 0.01$, *** $P < 0.001$ compared to the control group.

intracellular redox deviation in GO treated cells. Note that CCK-8 assay was more sensitive to alamarBlue because no significant change of cell survival rate was detected in alamarBlue assay following 40 μg/mL GO treatment for 6 h. Based on the above findings, we selected three concentrations of low, medium and high (40, 60, 80 μg/mL) to investigate potential adverse effect of GO in subsequent experiments. Next, we used flow cytometry to identify the possible patterns and types of cell death caused by GO. As demonstrated in Fig. 2D, a relatively higher dose of GO (80 μg/mL) resulted in apoptotic death in 38.2% of the total amounts of cells. However, there was almost no cell necrosis. This finding suggested that GO primarily induced apoptotic cell death in neural cell lines, which was supported by previous studies conducted by our group (Feng et al., 2018; Kang et al., 2017).

After determining the potential neurotoxic effects of GO, we studied the interaction between GO and cells using a phase-contrast microscope. Under physiological conditions, SH-SY5Y cells have two or more extending tentacles with intact edges. Following GO exposure for 24 h, numerous layered GO materials adhered to the cell surface, or inserted into the cell membrane, disrupting the integrity of cell edges (Fig. S2). Besides, GO materials were likely to agglomerate in the medium, forming large-size materials and accumulating around the cells. This adhesion behavior of GO may reduce the cellular uptake of nutrients from the surrounding culture medium, thus affecting cell growth and survival (Zhang et al., 2016). To further clarify the association of the plasma membrane with GO, cells were fixed in 4% PFA and observed under the SEM. As shown in Fig. 2E, a large number of GO materials adhered to the cell surface and even inserted into cell membranes. The hydrophobic interactions of graphene materials with the cell membrane could lead to cytoskeletal dysfunction and abnormal membrane permeability to a certain degree (Feng et al., 2018; Sasidharan et al., 2012). The biological interactions between GO with the plasma membrane were followed by possible cellular uptake (Zhang et al., 2016). Thereafter, FITC-labeled GO samples were prepared and co-cultured with cells for different time points for confocal microscopy observation. We found that the fluorescence intensity in cells enhanced with an increase in the incubation time, indicating an increase in cellular uptake

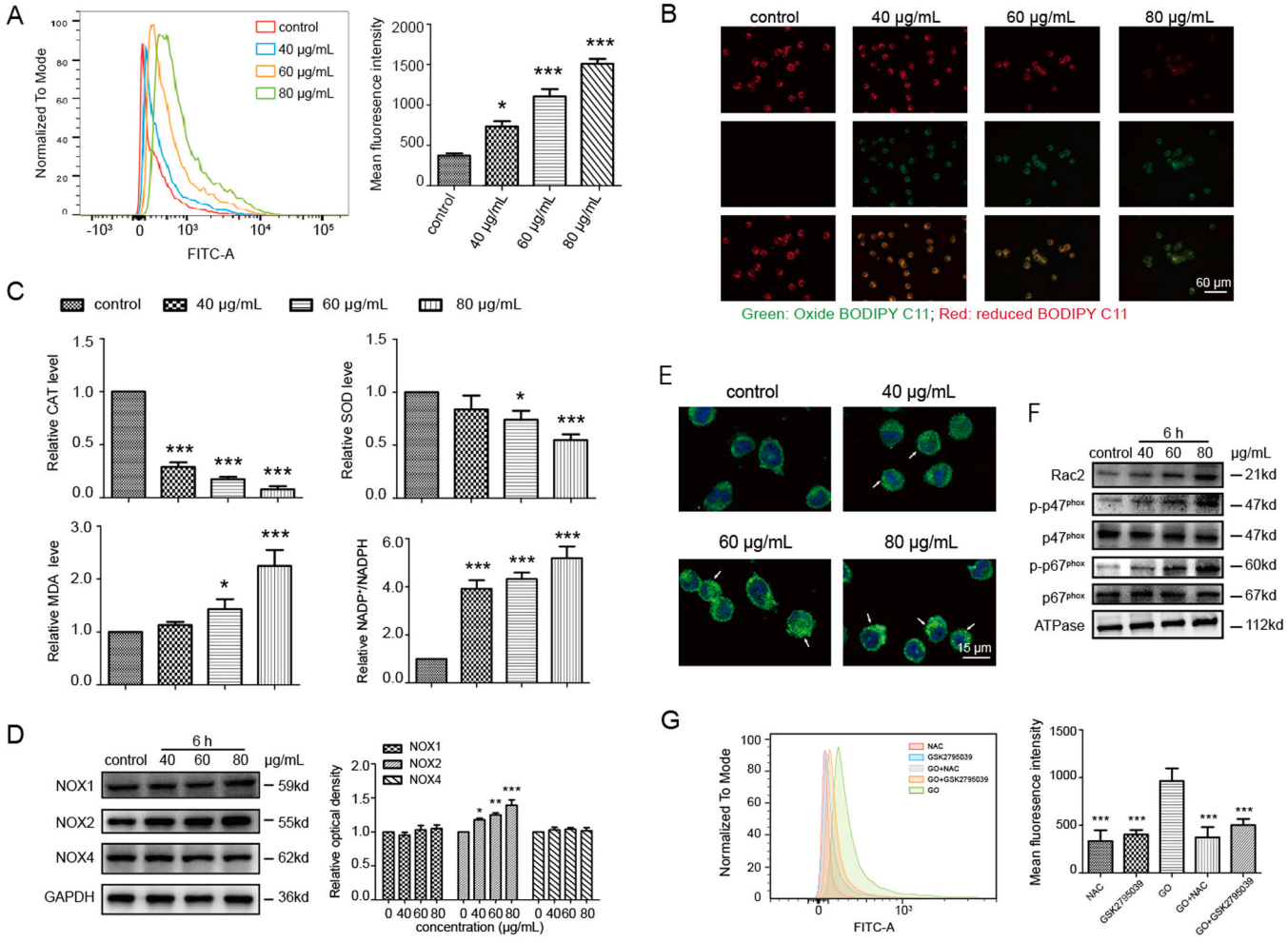

Fig. 3. Intracellular redox deviation induced by GO nanosheets. (A) Cells were incubated with 40, 60, 80 μg/mL GO for 6 h and stained with 10 μM DCFH-DA for 20 min and immediately detected using the flow cytometer. Intracellular ROS level was quantified via FITC fluorescence intensity and shown in the right histogram. (B) GO exposed cells were stained with 10 μM BODIPY 581/591 C11 peroxidation probe for 30 min and observed under the confocal microscope. The generation of lipid peroxidation was determined as the transition from red to green fluorescence. (C) Intracellular levels of CAT, SOD, MDA and $NADP^+$/NADPH content were also estimated to explore the status of oxidative stress. (D) Levels of NOX-related proteins (NOX1, NOX2 and NOX4) were detected via western blotting and GAPDH was used to determine the amount of loading control. The relative levels of indicated bands were shown in the right histograms. After exposure to GO samples for 6 h, the expression of NOX2 (defined as green fluorescence) in cells was observed under the confocal microscopy (E). (F) Translocation of NOX2 signaling to surface membrane in response to GO exposure were detected using western blotting. ATPase was used to determine the amount of loading proteins. (G) GO exposed cells were pretreated with/without NAC and NOX2 specific inhibitor (GSK2795038) and harvested for flow cytometer analysis. Intracellular ROS level was quantified via FITC fluorescence intensity and shown in the right histogram. All quantitative data are presented as mean ± SD of 3 independent tests, * $P < 0.05$, ** $P < 0.01$, *** $P < 0.001$ compared with the control group in (A), (C), (D), (F); *** $P < 0.001$ compared to GO treated cells in (H).

of GO (Fig. 2F). This finding was also confirmed by quantitative analysis using flow cytometry (Fig. S3). Considering that the intracellular green fluorescence could also be detected by materials adhering to the cell surface, direct observation of accumulation sites of GO in cells requires further studies.

3.3. Cellular redox deviation resulted from imbalanced antioxidant systems and activation of the NOX2 pathway

Through material characterization, we confirmed that GO nanosheets possessed potential pro-oxidative capability in biological environment. Thus we wonder how this property could react to the redox state inside the cell and further affect cell survival? Firstly, we measured the intracellular levels of ROS using the DCFH-DA assay and found that GO treatment elevated the cellular ROS in a concentration-dependent manner (Fig. 3A). Afterwards, we tested whether GO nanosheets triggered lipid peroxidation during the adhesion of these materials to the surface membrane. Cells were stained with BODIPY® 581/591 C11 reagent to observe fluorescence activity conversion from red to green. It was clear that a substantial switch to green fluorescence occurred in the plasma membrane of GO-treated cells (Figs. 3B and S4). It was interesting to note that oxidized graphene materials could strengthen membrane-disturbing abilities as compared with pristine graphene, thus damaging the membrane integrity (Mao et al., 2014; Kang et al., 2020). Excessive production of ROS could be an initial step in cellular oxidative stress. Several important biomarkers involved in the oxidative/antioxidative system were described in Fig. 3C. We detected a clear redox deviation inside cells, as evident from significantly reduced levels of CAT and SOD, which could catalyze superoxide anions and hydrogen peroxide (H_2O_2) to produce oxygen and water, respectively (Hao and Liu, 2019). The elevated content of intracellular MDA, the metabolic product of lipid peroxidation, was also in agreement with our above finding on membrane peroxidation. More importantly, we detected that the relative ratio of $NAPD^+$ to NADPH content increased remarkably with the increase in GO concentrations.

It has been reported that NADPH oxidase (NOX) can reduce oxygen molecules to superoxide anions through NADPH-dependent single-electron reduction, leading to ROS generation (Kalyanaraman et al., 2018). To further confirm the involvement of NOX enzymes in GO-driven cellular redox deviation, three important superoxide-producing NOX enzymes, including NOX1, NOX2, and NOX4 (Ma et al., 2018) were identified by western blotting. Compared to its counterparts, only the expression of NOX2 increased in cells exposed to GO (Fig. 3D). Further, this finding was supported by immunofluorescence analysis as shown in Figs. 3E and S5. The phagocyte NOX2 is widely known for its function in immune defense; however, recent evidence pointed out that non-phagocytized NOX2 distributed in neuronal systems also played essential roles in cellular oxidative stress (Kang et al., 2020). The NADPH activity is associated with the unique binding between NOX isoforms and NOX-related regulatory subunits. The specific binding partners of NOX2 (also named as $gp91^{phox}$) include phosphorylated $p67^{phox}$ and $p47^{phox}$, which could translocate to the plasma membrane along with a Rac1/2-containing complex upon activation (Martner et al., 2019). We analyzed the extracted cell membrane proteins by western blotting and detected increasing expressions of RAC2, phosphorylated $p67^{phox}$ and $p47^{phox}$, which confirmed the effective activation of NOX2 enzyme complex following GO exposure (Figs. 3F and S6). Finally, we used flow cytometry to check whether the treatment of GSK2795038, a specific inhibitor of NOX2, could inhibit ROS generation. As shown in Fig. 3G, elevated levels of ROS following GO treatment were reduced by GSK2795038 incubation, exerting an effect similar to that of NAC (total ROS scavenger) treatment. The selection of effective NAC concentration (600 μM) was shown in Fig. S7. Together, our data illustrated the intrinsic mechanism of GO-induced redox deviation in SH-SY5Y cells, that was primarily resulted from activation of the NOX2 signaling pathway and weakened antioxidant capacity.

3.4. Induction of apoptosis was linked to ROS-derived mitochondrial stress

Mitochondria serve as the primary energy providers within cells; however, their metabolic processes such as oxidative phosphorylation also produce ROS, leaving them vulnerable to other forms of oxidative stress (Yang et al., 2016). The normal opening of mPTP is necessary for maintaining the membrane potential and energy metabolism of mitochondria (Tsutsumi and Sasase, 2019). This study first investigated whether GO-drived ROS could enhance mPTP activation using a commercial fluorescent reagent, calcein-AM (Li et al., 2019) that could be passively transported into the cells and aggregated in mitochondria (Fig. 4A). Under physiological conditions, closed mPTP prevents the quenchant, $CoCl_2$, from entering the mitochondria, such that only mitochondria exhibit strong green fluorescence in the calcein + medium group. Nevertheless, the fluorescence intensity decreased significantly in GO-exposed cells in a concentration-dependent manner, revealing a similar effect compared with positive Ionomycin treatment (Fig. 4B). These observations confirmed that GO resulted in continuous opening of mPTP, changing the normal mitochondrial permeability, which may accelerate the progression of mitochondrial stress and initiate apoptotic cell death (Chen et al., 2018; Zhang et al., 2018). From the data shown in Fig. 4C, exposure to GO substantially reduced $\Delta\Psi m$ by a maximum of 60% as compared with control cells, which was quantified as the relative ratio of red to green fluorescence intensity (Fig. 4D).

The electron transfer process of the mitochondrial respiratory chain (also called electron transport chain, ETC) is coupled to ADP phosphorylation, also known as oxidative phosphorylation. The mitochondrial ETC consists of two respiratory chains depending on the hydrogen donor, NADH or $FADH_2$. However, only the former is responsible for ATP synthesis (Guo et al., 2018). Therefore, we examined enzymatic activities of three typical complexes, namely complex I, complex III, and complex IV, in the NADH respiratory chain. The activity of these complexes decreased remarkably after GO treatment in a concentration-dependent manner (Fig. 4E). Furthermore, we detected a significant blockage of ATP synthesis along with an increase in AMP content in response to GO stimulation, as evidenced in Fig. 4F. Based on these findings, we believe that the abnormal activation of mPTP uncouples oxidative phosphorylation in the mitochondria. Other types of nanomaterials, such as nano-TiO_2 (Geng et al., 2020) and -Mn (Alaimo et al., 2014) were also reported to cause mPTP abnormally open and mitochondrial disruption. To further investigate the function of mtROS in the cellular redox system, cells were stained with MitoSOX, a specific mitochondria-targeted probe, and observed under a fluorescence microscope. GO stimulation significantly enhanced the fluorescence intensity in cells, which correlated with the quantitative analysis by flow cytometry (Figs. S8 and 4G).

Over-opening of mPTP leads to increased mitochondrial permeability and the release of pro-apoptotic factors such as cytochrome C into the cytoplasm, which further activates intrinsic apoptotic pathways (Xiao et al., 2018). Therefore, the relative levels of CytC in the mitochondria and the cytoplasm were respectively detected by western blotting. As shown in Fig. 4H, the CytC content in the mitochondria decreased, whereas its content increased in the cytoplasm following GO treatment. This result confirmed our speculation that GO induced distinct translocation of CytC from the mitochondria to the cytoplasm. Subsequently, we assessed the potential pathways involved in intrinsic cell apoptosis. Western blotting revealed that the level of pro-apoptotic protein, Bax, increased markedly following GO treatment for 24 h. In addition, the levels of phosphorylated Caspase 9 and Caspase 3 increased significantly in a concentration-dependent manner (Fig. 4I). Apoptosis occurs in a cascade of proteases mediated by members of the caspase family. Among them, activation of primordial caspase 9 can activate downstream caspase3 and directly play a pro-apoptotic role (Wang et al., 2019). The mitochondrial intrinsic pathway has also been identified to regulate apoptosis induced by other types of nanomaterials

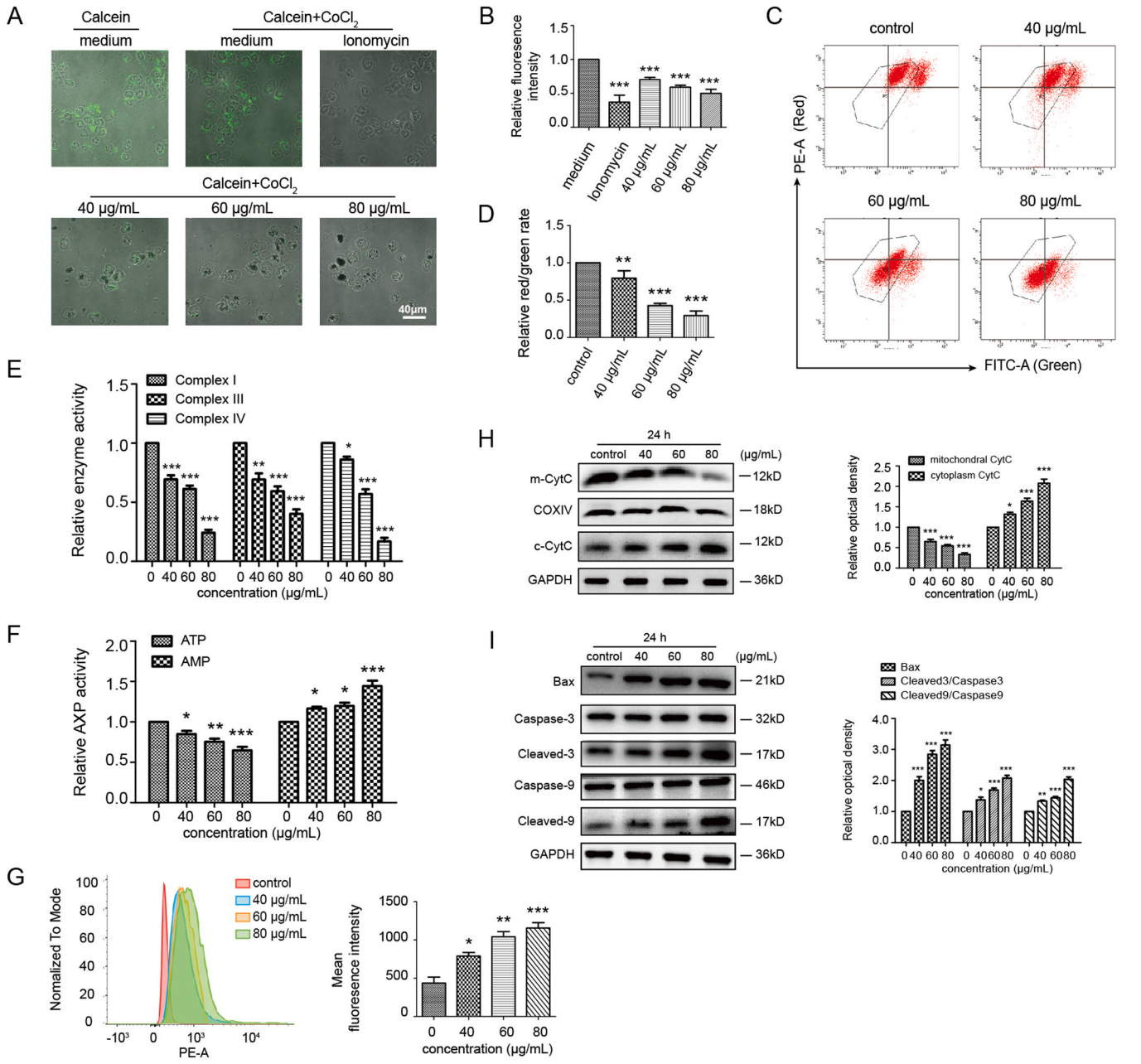

Fig. 4. GO impaired mitochondrial homeostasis in SH-SY5Y cells. (A) The changes of mitochondrial membrane permeability were observed by confocal microscopy in GO treated cells following 24 h exposure. Ionomycin (0.5 μM) was used as a positive treatment. The relative fluorescence intensity was analyzed and presented in (B). (C) Cells were stained with JC-1 working solution for 20 min at 37 °C and analyzed with a flow cytometry. The relative ration of red to green fluorescence was analyzed and presented in (D). (E) Enzymatic activity changes of three typical mitochondrial respiratory chain complexes (complex I, complex III and complex IV) in GO treated cells. (F) Cellular content of AMP and ATP in GO treated cells. Cells were stained with a MitoSOX red indicator and harvested for flow cytometry analysis. The mean fluorescence intensity was quantified and presented in the right histograms (G). (H) Plasma protein and mitochondrial protein were extracted from GO exposed cells and subjected to western blotting. GAPDH and COXIV was respectively used as a loading control for plasma protein and mitochondrial protein. Relative levels of CytC were shown in the right histograms. (I) Cellular total proteins were harvested for western blotting analysis and GAPDH was used as a loading control. The relative levels of indicated bands were shown in the right histograms. Values are presented as mean ± SD of 3 independent tests, * $P < 0.05$, ** $P < 0.01$, *** $P < 0.001$ compared to the control group.

such as cuprous oxide (Yang et al., 2017), zinc oxide (Xiaoli et al., 2017), and silica nanoparticles (Guo et al., 2018). Meanwhile, note that ROS-mediated oxidative stress can cause other types of secondary effects, which are not always related to cell death (Zhang et al., 2016; Stefanatos and Sanz, 2018; Kunovac et al., 2019; Liang et al., 2019). Collectively, we found that cellular redox deviation correlated with the occurrence of mitochondrial stress, eventually triggering the observed apoptotic cell death in response to GO exposure.

3.5. Mitochondrial dysfunction activated autophagy through the AMPK/mTORC1/ULK1 pathway

Apart from triggering apoptosis, stressed mitochondria may activate autophagy to self-preserve (Yamashita and Kanki, 2017). As mentioned above, the disruption of mitochondrial ETC creates an imbalance in cellular energy metabolism as manifested by a turnover ratio of AMP to ATP content. Consequently, we studied whether AMP-activated protein kinase (AMPK), which modulates metabolic homeostasis by sensing the

cellular energy status, participated in initiating the autophagy flux. Western blotting results demonstrated that the levels of phosphorylated AMPK (pAMPK) and ULK1 (pULK1) increased, whereas those of phosphorylated mTORC1 (pmTORC1) decreased (Fig. 5A) in GO-treated cells. Cells regulate the phosphorylation of ULK1 under different physiological conditions through AMPK and mTORC1 signaling, thus sensing the energy changes to modulate autophagy (Holczer et al., 2019). To directly observe the formation of autophagosomes, cells were fixed in 2.5% glutaraldehyde and observed under the TEM (Fig. 5B). We detected the formation of numerous autophagosomes or autolysosomes in the cytoplasm of cells exposed to GO (shown by the black arrow), some of which contained GO nanosheets (shown by the white arrow) taken up by cells. This internalization of graphene materials has also been observed in other cell types despite different cellular uptake patterns (Ma et al., 2015; Xu et al., 2016; Contreras-Torres et al., 2017). Moreover, ultrastructural changes in mitochondria, including vacuolated mitochondria and breakage of mitochondrial cristae (shown by the black triangle), were detected in the experimental group. These findings strengthened the potential link between the initiation of autophagy and mitochondrial dysfunction.

The occurrence of autophagy (also known as autophagy flux) undergoes several dynamic processes, including the formation of the initial sequestering compartment, autophagosome maturation, the fusion between the autophagosome and lysosome, and degradation within autolysosomes. Several proteins involved in regulating the autophagy machinery, for example, autophagy-related protein 5 (Atg5), microtubule-associated protein 1 light chain 3 (LC3), and Beclin1 (mammalian Atg6) are crucial for autophagosome synthesis (Han et al., 2019). It is well known that the conversion from LC3-I to LC3-II is a hallmark of autophagy initiation, which was demonstrated as an increase in the relative ratio of LC3-II/LC3-I (Fig. 5C). Moreover, western blotting revealed distinct upregulation of Atg5 and Beclin1. We further validated our findings using another imaging approach to observe the formation of LC3-positive autophagosomes (Fig. 5D). A

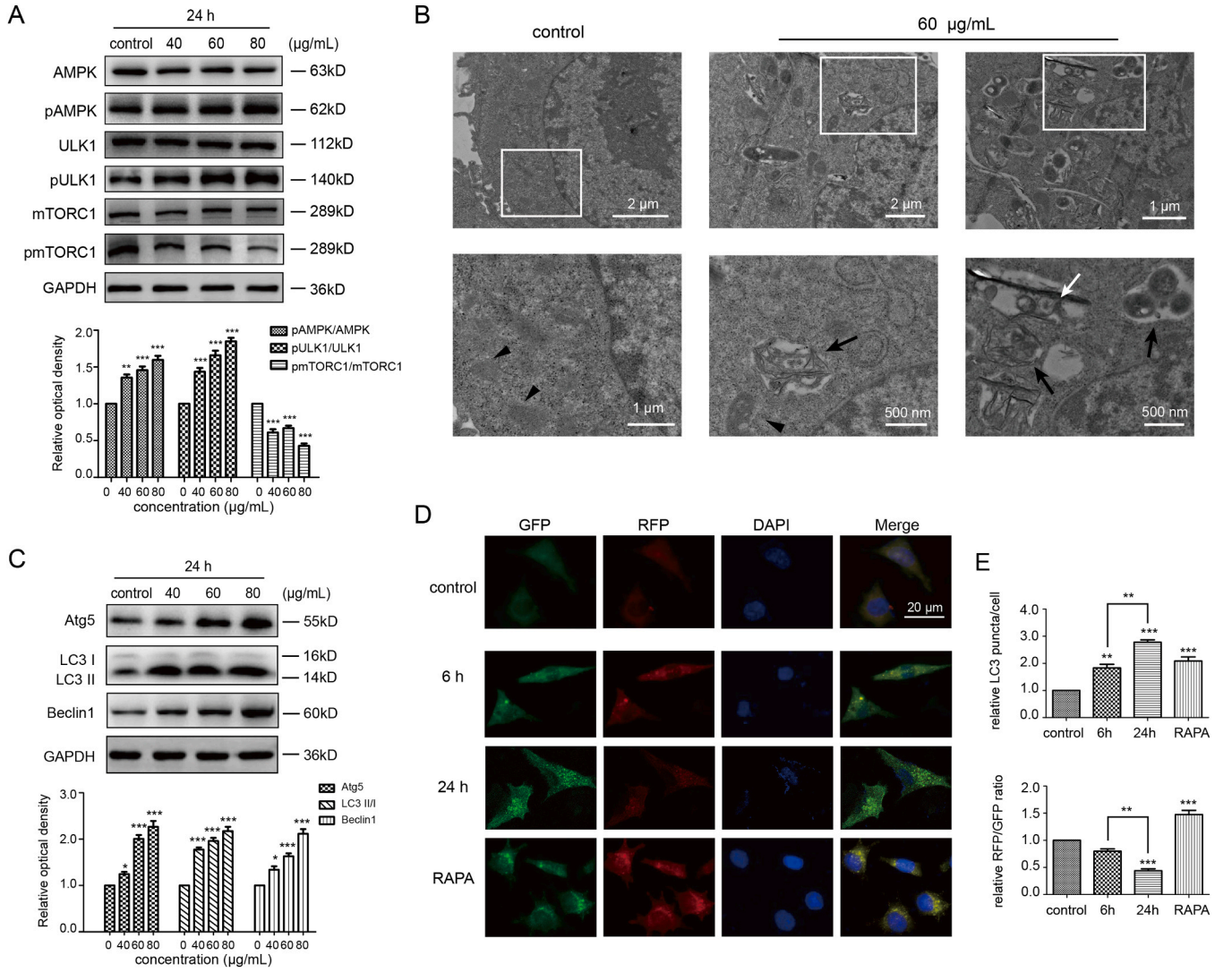

Fig. 5. Induction of autophagy by mitochondria stress was linked to AMPK/mTORC1/ULK1 pathway. Total proteins were extracted from cells treated with 40, 60, 80 μg/mL GO for 24 h, and subjected for western blotting analysis. GAPDH was used to determine the amount of loading proteins. Relative levels of AMPK, ULK1, mTORC1 proteins and their phosphorylated counterparts were quantified and presented in (A); Relative levels of Atg5, LC31, LC3II, and Beclin1 proteins were quantified and presented in (C); (B) GO treated cells were harvested for TEM observation. The below images were magnifications of the white boxes in upper images, which reveled the mitochondria (black triangle), autophagic vacuoles (black arrows) and GO sheets (white arrows). Cells expressing stubRFP-sensGFP-LC3were exposed to 60 μg/mL GO for 6 or 24 h. RAPA (100 nM) was used a positive control. Formations of autophagosomes and autolysosomes were detected by the confocal microscope (D). The relative LC3 puncta/cell and RFP to GFP fluorescence intensity ratio was respectively analyzed and shown in (E). Values are presented as mean ± SD of 3 independent tests, * $P < 0.05$, ** $P < 0.01$, *** $P < 0.001$ compared to the control group.

lentivirus-transfected cell line stably expressing RFP-GFP fluorescent-tagged LC3 was exposed to GO or RAPA (100 nM) for different time points and observed using confocal microscopy. LC3-positive puncta in the autophagosomes showed a merged signal of GFP and RFP, whereas the fluorescence signal mainly switched to RFP in the autolysosomes because of the acidic environment within the lysosomes. More evident accumulation of LC3-positive puncta was detected in cells following incubation with GO or RAPA, suggesting enhanced autophagosome synthesis. We noted that the relative RFP/GFP ratio reduced in GO-exposed cells as compared with that in the RAPA group, which, on

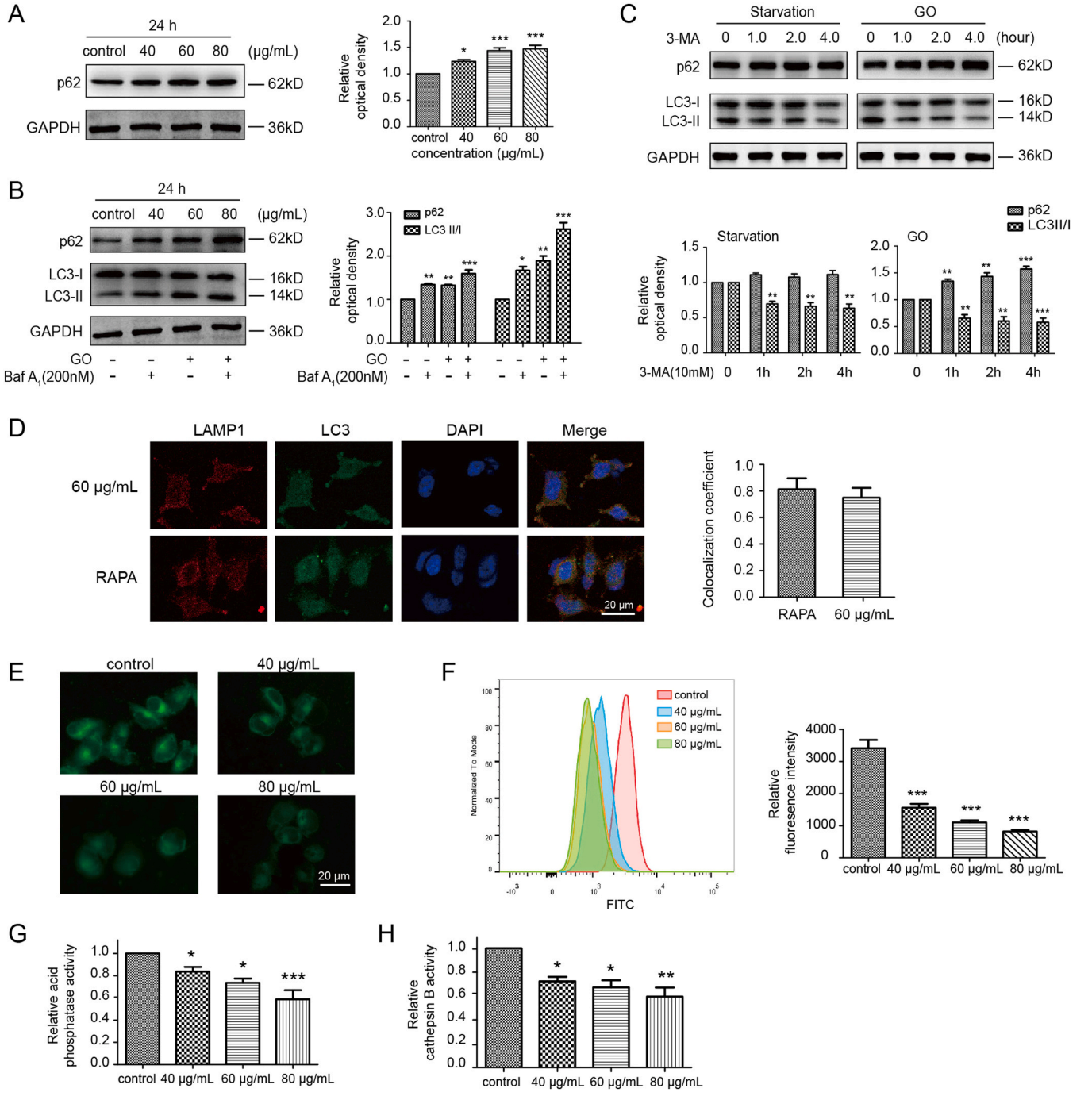

Fig. 6. Blockade of autophagic flux was resulted from impaired lysosomal degradation. (A) After GO stimulation, the expression of p62 protein was detected via western blotting. GAPDH was used to identify the amount of loading proteins. (B) Cells were exposed to GO with/without Baf A_1 (200 nM) for 24 h and subjected to western blotting. The relative levels of p62 and LC3 II/LC3 I were shown in the right histograms. (C) Cells were pretreated with 60 μg/mL GO or incubated with starvation medium for 24 h and then exposed to 10 mM 3-MA for 1, 2, 4 h. At indicated time points, total proteins were harvested for western blotting. Relative levels of p62 and LC3 II/LC3 I were shown in the bottom histograms. (D) Cells were incubated with 60 μg/mL GO or 100 nM RAPA for 24 h and stained with mouse anti-LAMP1 (red) and rabbit anti-LC3 (green) antibodies. The confocal microscope was employed to observe colocalization of LAMP1 and LC3 positive puncta. The fluorescence activity was quantified by ImageJ (right). (E) LysoSensor Green probe was used to identify lysosomes and imaged under a fluorescent microscope. Additionally, the flow cytometry was used to quantitatively evaluate the intensity of FITC fluorescence (F). The enzymatic activity of acid phosphatase enzyme (G) and cathepsin B (H) were respectively detected to identify lysosomal degradative capacity. Values are presented as mean ± SD of 3 independent tests, * $P < 0.05$, ** $P < 0.01$, *** $P < 0.001$ compared with control group.

the contrary, indicated a block of autophagic flux in the terminal stage. Efficient autophagy is crucial for maintaining mitochondrial homeostasis via the timely elimination of dysfunctional mitochondria to avoid further damage to cells (Wu et al., 2019). Autophagy block may lead to excessive accumulation of stressed, ROS-generating mitochondria, which in turn, enhances oxidative damaging the healthy mitochondria.

3.6. Autophagy flux block resulted from weak lysosomal degradative capacity

Autophagy is a fundamental process that degrades impaired cellular components and protein aggregates at basal levels, but any abnormity of the pathway may participate in nanomaterial toxic effects (Mohammadinejad et al., 2019; Feng et al., 2020). To further identify the specific sites of the abnormal autophagic pathway, the level of p62 protein, a substrate that is preferentially degraded by autophagy, was determined using western blotting (Fig. 6A). The results revealed that GO treatment increased the p62 levels in a concentration-dependent manner, indicating inhibition of normal degradation. Subsequently, we used two types of inhibitors that affected autophagy machinery to analyze the role of GO exposure in the progress of autophagic flux. First, cells were treated with GO in the presence or absence of Baf A_1, an inhibitor affecting the acidity of lysosomes (Mauvezin and Neufeld, 2015), and harvested for western blotting. GO exerted an effect similar to that exerted by Baf A_1, which simultaneously enhanced the intracellular levels of LC3 II/I and p62 protein (Fig. 6B). Afterwards, we investigated the degradation levels of autophagy substrates by treating the cells with 3-MA (Sun et al., 2018) to inhibit the formation of new autophagosomes. Following the treatment with 3-MA, the ratio of LC3-II/LC3I decreased dramatically in both starved and GO-exposed cells, which resulted from effective inhibition of autophagy in the initial stage. However, we noted that GO increased the p62 levels in a dose-dependent manner in contrast to stable p62 levels in starved cells, suggesting the existence of weakened autophagic degradation following GO treatment (Fig. 6C). The terminal stage of autophagy involves two steps: the fusion of the autophagosome with the lysosome and subsequent cargo degradation (Feng et al., 2020). Therefore, the autophagosome–lysosome fusion was further assessed by observing the colocalization of GFP-tagged LC3 and RFP-tagged LAMP1. The fluorescent images revealed that the colocalization of LC3 and LAMP1 in GO-treated cells was almost identical to that in the RAPA group (Fig. 6D). Thus, the fusion between the autophagosome and lysosome was not affected by GO treatment.

To further verify the possibility of impairment within lysosomes, we investigated the acidification of lysosomes, which is critical for lysosomal maturation and activating a majority of lysosomal hydrolases. Cells were stained with a pH-dependent lysosensor for microscopic observation. The fluorescence intensity was quantified by flow cytometry. We detected that the fluorescence intensity in GO-treated cells reduced remarkably (Fig. 6E, F), suggesting an increased lysosome pH. A high acidic pH (between 4.5 and 5.0) inside the organelle lumen is required to activate the hydrolytic enzymes within the lysosomes (Mindell, 2012). Consequently, we examined the activity of two representative lysosomal enzymes, ACP and cathepsin B. We found a clear decrease in the enzymatic activity following treatment with GO (Fig. 6G, H). As mentioned in the previous section, the activation of the AMPK/ULK1 pathway is required for inducing autophagy in response to GO stimulation. Note that the activation of AMPK signaling can prevent lysosome acidification through inhibition of vaculolar ATPase (vATPase) assembly, which might explain the observed lysosomal dysfunction (Nwadike et al., 2018). From a mechanistic point of view, we proposed that GO impaired the autophagic degradative capacity by steric hindrance due to their persistent presence within the lysosomes as a kind of non-degradable material. Furthermore, the phenomenon has been reported in other non-biodegradable nanomaterials such as nano carbon black (CBNPs) (Guan et al., 2020) and SiO_2 nanoparticles (Manshian et al., 2018).

3.7. Inhibition of ROS signaling and lysosomal reacidification alleviated GO-induced mitochondrial stress

We observed intracellular redox deviation and subsequent autophagy–lysosomal network dysfunction following GO stimulation. To further verify our speculations regarding the mechanism of action of GO-triggered adverse effects in SH-SY5Y cells, we conducted rescue experiments using specific chemical reagents. First, NAC, a ROS scavenger, was introduced to GO-exposed cells to observe the alterations in cell viability using the CCK-8 assay. We detected that NAC significantly increased the cellular survival rates as compared to single GO treatment under different concentrations (Fig. 7A). This finding supported the fact that GO-derived ROS generation resulted in oxidative cell damage. We next examined whether NAC could alleviate ROS-targeted mitochondrial injury. As shown in Figs. 7B and S9 (statistical analysis of flow cytometry data), the combined treatment of NAC with GO weakened the evident loss of mitochondrial membrane potential in the GO group. As expected, the abnormal turnover of AMP and ATP content resulting from mitochondrial uncoupling recovered in response to treatment with NAC (Fig. 7C).

Afterward, we applied the cAMP cocktail to restore lysosomal pH and evaluated its potential function in lysosomal acidification, autophagic flux, and cell survival following GO stimulation. Based on the fluorescence images shown in Fig. 7D, the fluorescence intensity of green DND-189 in GO-exposed cells increased remarkably (Fig. S10) following the addition of cAMP, suggesting effective acidification of lysosomal pH. We next used LC3 lentivirus-transfected cells to observe the progress of autophagic flux; the results showed that the reduced levels of RFP/GFP following GO stimulation greatly improved after co-incubation with cAMP (Figs. 7E and S11). Again, this observation supported our hypothesis that GO-mediated alkalizing effect in the lysosomes and the subsequent impaired degradative capacity blocked the autophagy pathway. More importantly, the elimination of dysfunctional mitochondria via autophagy recovered to the basal levels as demonstrated by the TEM images. More healthy mitochondria (shown in black triangle) were detected in the cytoplasm in GO exposed cells in the presence of cAMP treatment (Fig. 7F). These findings well explained the increased cell viability following treatment with a combination of GO and cAMP (Fig. 7G). Finally, we provided evidence that the CytC–Bax–Caspase signaling pathway was involved in GO-induced apoptosis by activating ROS signaling. This intrinsic apoptotic pathway could be abolished through the effective degradation of abnormal mitochondria by the autophagy–lysosome system. Co-treatment with NAC or cAMP with GO effectively inhibited GO-triggered elevated apoptosis rate (Fig. 7J), manifested as decreased CytC release from the mitochondria to the cytoplasm, and downregulated levels of Bax and phosphorylated Caspase 9 and 3 proteins (Figs. 7H, I and S12) by western blotting.

4. Conclusions

This study mainly described how complicated GO chemistry engages neural cell line. Before administration to cells, GO was characterized in detail including their microstructure, zeta potential, dispersion in the medium as well as its oxidation status, and surface reactivity. Carbon and hydroxyl radicals were detected on the GO surface upon ultrasonic treatment, further triggering lipid peroxidation of the plasma membrane in SH-SY5Y cells. After cellular uptake, GO induced redox deviation by activating the NOX2 pathway in combination with imbalanced antioxidant systems. Elevated ROS caused the continuous opening of mPTP, leading to a sequence of events linked to mitochondrial stress, including a reduction in $\Delta\Psi m$, uncoupling of ETC, turnover of AMP/ATP ratio, and generation of mtROS. Subsequently, AMPK sensed the compromised energy status and activated autophagy by regulating the AMPK/mTOR/ULK1 pathway. In addition, GO exposure induced an alkalizing effect in the lysosomes, impairing the normal progression of autophagic flux and limiting the clearance of autophagosomes, finally resulting in over-

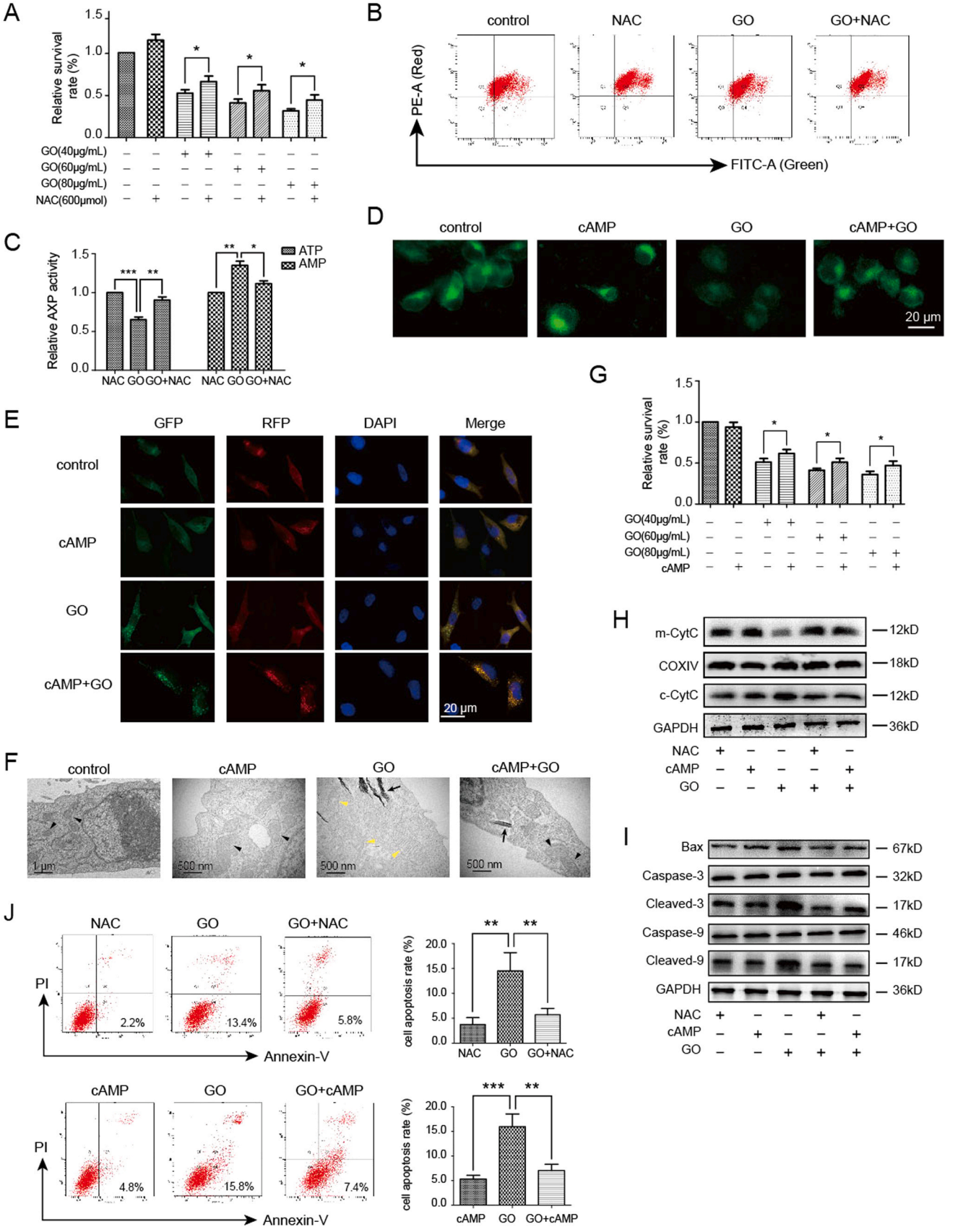

(caption on next page)

Fig. 7. Inhibition of ROS signaling and lysosomal reacidification alleviated mitochondrial injury. (A) Cells were treated with 40, 60, 80 μg/mL GO in the presence or absence of 600 μM NAC for 24 h and subjected to CCK-8 assay. (B) Flow cytometry analysis of ΔΨm in 60 μg/mL GO exposed cells with or without NAC co-incubation. (C) Intracellular content of AMP and ATP in 60 μg/mL GO exposed cells with or without NAC co-incubation. (D) Additionally, cells were treated with 60 μg/mL GO in the presence or absence of cAMP for 24 h and stained with LysoSensor Green probe. Cells were then imaged using a fluorescent microscope and relative fluorescence intensity was shown in the in the right histograms. (E) Cells transfected with LC3 lentivirus were exposed to GO in the presence or absence of cAMP for 24 h. Nuclei were labeled with DAPI (blue). Formations of autophagosomes and autolysosomes were observed by the confocal microscope. (F) TEM observation of GO exposed cells with or without cAMP co-incubation. The black triangle indicates healthy mitochondria and yellow triangle indicates damaged mitochondria, and black arrow indicates internalized GO samples. (G) Cell viability assay after exposure to 40, 60, 80 μg/mL GO in the presence or absence of cAMP cocktail for 24 h. Finally, GO exposed cells were treated with/without NAC or cAMP co-incubation in the same time. (H) Relative levels of CytC in plasma protein and mitochondrial protein were detected via western blotting analysis. (I) Cells were treated with 60 μg/mL GO for 24 h and total proteins were also harvested for western blotting to detect relative levels of Bax, cleaved Caspase 3 and cleaved Caspase 9. (J) Cells were stained with the Annexin-V/PI dye and the apoptosis rate was analyzed using a flow cytometry. Values are presented as mean ± SD of 3 independent tests, * $P < 0.05$, ** $P < 0.01$, *** $P < 0.001$.

accumulation of autophagy-related substrates including dysfunctional mitochondria. Altogether, these toxic effects triggered mitochondria-mediated apoptotic cell death by activating the CytC–Bax–Caspase signaling (Fig. 8). *In vitro* toxicological pathways could be remarkably abolished by the addition of NAC or cAMP. These data highlighted the significance of structure-related activity of GO on its biological behavior and provided an in-depth understanding of how GO-derived cellular redox signaling could modulate cell functionality and survival, contributing for the prevention of GO exposure risks in neuromedical fields.

Funding

This work was supported by the National Natural Science Foundation

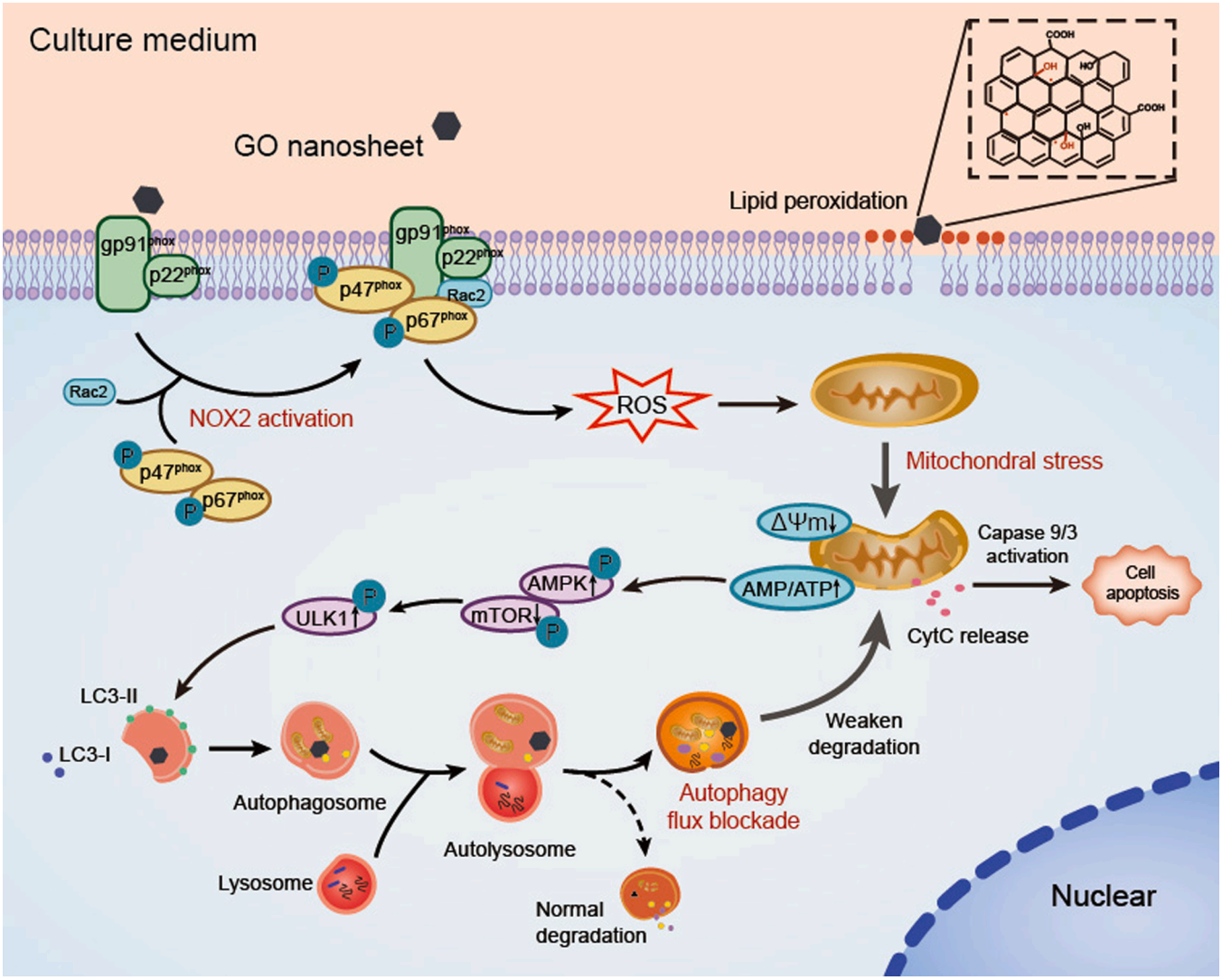

Fig. 8. Schematic model for the mechanism of GO-disrupted mitochondrial homeostasis. GO interactered with cell membrane and triggered lipid peroxidation in SH-SY5Y cells. After internalization, GO induced intracellular redox deviation through activation of NOX2 pathway. GO-drived ROS impaired mitochondrial homeostasis and induced a significant increase in the ratio of AMP/ATP. AMPK signaling sensed the imbalanced energy status and further activated autophagy through inhibition of mTORC1. The autophagy flux was initiated as a defensive reaction to obliterate oxidative damaged mitochondria and foreign nanomaterials, which whereas revealed to be ineffective due to impaired lysosomal degradative capacity. These sequential cellular responses further exacerbated mitochondrial stress, leading to the release of CytC and activation of Caspase 9 and 3, eventually caused apoptotic cell death.

of China (81870786, 52072167, 82001298, 81701026), China Postdoctoral Science Foundation funded project (2019M662986), Guangdong Basic and Applied Basic Research Foundation (2019A1515110635), Medical Scientific Research Foundation of Guangdong Province of China (A2020131), Science research cultivation program of stomatological hospital, Southern Medical University (PY2019006).

CRediT authorship contribution statement

Feng Xiaoli: Methodology, Conceptualization, Data curation, Investigation, Visualization, Writing - original draft, Writing - review & editing. **Zhang Yaqing**: Methodology, Data curation, Investigation, Validation, Visualization. **Luo Ruhui**: Methodology, Investigation. **Lai Xuan**: Investigation, Visualization. **Chen Aijie**: Methodology, Writing - review & editing. **Zhang Yanli**: Methodology, Writing - review & editing. **Hu Chen**: Methodology, Visualization. **Chen Lili**: Conceptualization, Supervision. **Shao Longquan**: Funding acquisition, Supervision, Project administration.

Authors' contributions

Shao Longquan conceived this study. Feng Xiaoli, Zhang Yaqing, Luo Ruhui, Chen Aijie, Zhang Yanli performed in vitro experiments. Feng Xiaoli, Lai Xuan and Hu Chen performed the nanomaterial characterization. Feng Xiaoli and Zhang Yaqing conducted data analysis. Chen Lili contributed to the design of the experiment. The manuscript was written by Feng Xiaoli and verified by Zhang Yaqing.

Consent for publication

All the authors consent for publication.

Declaration of Competing Interest

No potential conflict of interest was reported by the authors.

Appendix A. Supporting information

Supplementary data associated with this article can be found in the online version at doi:10.1016/j.jhazmat.2021.126158.

References

Alaimo, A., Gorojod, R.M., Beauquis, J., Muñoz, M.J., Saravia, F., Kotler, M.L., 2014. Deregulation of mitochondria-shaping proteins Opa-1 and Drp-1 in manganese-induced apoptosis. PLOS One 9 (3), 91848. Mar 14.

Atiroglu, V., 2020. Lipase immobilization on synthesized hyaluronic acid-coated magnetic nanoparticle-functionalized graphene oxide composites as new biocatalysts: improved reusability, stability, and activity. Int. J. Biol. Macromol. 145, 456–465.

Bonnier, F., Keating, M.E., Wróbel, T.P., Majzner, K., Baranska, M., Garcia-Munoz, A., Blanco, A., Byrne, H.J., 2015. Cell viability assessment using the Alamar blue assay: a comparison of 2D and 3D cell culture models. Toxicol. Vitro 29, 124–131.

Cadenas, S., 2018. Mitochondrial uncoupling, ROS generation and cardioprotection. Biochim Biophys. Acta Bioenerg. 1859 (9), 940–950.

Chen, S., Lv, X., Hu, B., Zhao, L., Li, S., Li, Z., Qing, X., Liu, H., Xu, J., Shao, Z., 2018. Critical contribution of RIPK1 mediated mitochondrial dysfunction and oxidative stress to compression-induced rat nucleus pulposus cells necroptosis and apoptosis. Apoptosis 23, 299–313.

Chen, X., Liu, C., Huang, Z., Pu, X., Shang, L., Yin, G., Xue, C., 2019. Preparation of carboxylic graphene oxide-composited polypyrrole conduits and their effect on sciatic nerve repair under electrical stimulation. J. Biomed. Mater. Res. A 107, 2784–2795.

Coffey, E.E., Beckel, J.M., Laties, A.M., Mitchell, C.H., 2014. Lysosomal alkalization and dysfunction in human fibroblasts with the Alzheimer's disease-linked presenilin 1 A246E mutation can be reversed with cAMP. Neuroscience 263, 111–124.

Contreras-Torres, F.F., Rodríguez-Galván, A., Guerrero-Beltrán, C.E., Martínez-Lorán, E., Vázquez-Garza, E., Ornelas-Soto, N., García-Rivas, G., 2017. Differential cytotoxicity and internalization of graphene family nanomaterials in myocardial cells. Mater. Sci. Eng. C Mater. Biol. Appl. 73, 633–642.

Feng, X., Chen, A., Zhang, Y., Wang, J., Shao, L., Wei, L., 2015. Central nervous system toxicity of metallic nanoparticles. Int J. Nanomed. 10, 4321–4340.

Feng, X., Chen, L., Guo, W., Zhang, Y., Lai, X., Shao, L., Li, Y., 2018. Graphene oxide induces p62/SQSTM-dependent apoptosis through the impairment of autophagic flux and lysosomal dysfunction in PC12 cells. Acta Biomater. 81, 278–292.

Feng, X., Zhang, Y., Zhang, C., Lai, X., Zhang, Y., Wu, J., Hu, C., Shao, L., 2020. Nanomaterial-mediated autophagy: coexisting hazard and health benefits in biomedicine. Part. Fibre Toxicol. 17, 53.

Geng, R., Ren, Y., Rao, R., Tan, X., Zhou, H., Yang, X., Liu, W., Lu, Q., 2020. Titanium dioxide nanoparticles induced HeLa cell necrosis under UVA radiation through the ROS-mPTP pathway. Nanomaterials 10 (10), 2029.

Gies, V., Zou, S., 2018. Systematic toxicity investigation of graphene oxide: evaluation of assay selection, cell type, exposure period and flake size. Toxicol. Res. 7, 93–101.

Guan, S., Tao, S., Huang, Y., Jin, Y., Hu, Y., Lu, J., 2020. Combined toxic effects of CBNPs and Pb on rat alveolar macrophage apoptosis and autophagy flux. Ecotoxicol. Environ. Saf. 205, 111062.

Guo, C., Ma, R., Liu, X., Xia, Y., Niu, P., Ma, J., Zhou, X., Li, Y., Sun, Z., 2018. Silica nanoparticles induced endothelial apoptosis via endoplasmic reticulum stress-mitochondrial apoptotic signaling pathway. Chemosphere 210, 183–192.

Guo, R., Gu, J., Zong, S., Wu, M., Yang, M., 2018. Structure and mechanism of mitochondrial electron transport chain. Biomed. J. 41, 9–20.

Guo, Z., Xie, C., Zhang, P., Zhang, J., Wang, G., He, X., Ma, Y., Zhao, B., Zhang, Z., 2017. Toxicity and transformation of graphene oxide and reduced graphene oxide in bacteria biofilm. Sci. Total Environ. 580, 1300–1308.

Han, X., Sun, S., Sun, Y., Song, Q., Zhu, J., Song, N., Chen, M., Sun, T., Xia, M., Ding, J., Lu, M., Yao, H., Hu, G., 2019. Small molecule-driven NLRP3 inflammation inhibition via interplay between ubiquitination and autophagy: implications for Parkinson disease. Autophagy 15, 1860–1881.

Hao, M., Liu, R., 2019. Molecular mechanism of CAT and SOD activity change under MPA-CdTe quantum dots induced oxidative stress in the mouse primary hepatocytes. Spectrochim. Acta A Mol. Biomol. Spectrosc. 220, 117104.

Henson, T.E., Navratilova, J., Tennant, A.H., Bradham, K.D., Rogers, K.R., Hughes, M.F., 2019. In vitro intestinal toxicity of copper oxide nanoparticles in rat and human cell models. Nanotoxicology 13, 795–811.

Holczer, M., Hajdu, B., Lorincz, T., Szarka, A., Banhegyi, G., Kapuy, O., 2019. A double negative feedback loop between mTORC1 and AMPK kinases guarantees precise autophagy induction upon cellular stress. Int. J. Mol. Sci. 20.

Holmes, A.M., Mackenzie, L., Roberts, M.S., 2020. Disposition and measured toxicity of zinc oxide nanoparticles and zinc ions against keratinocytes in cell culture and viable human epidermis. Nanotoxicology 14, 263–274.

Hsieh, H.S., Wu, R., Jafvert, C.T., 2014. Light-independent reactive oxygen species (ROS) formation through electron transfer from carboxylated single-walled carbon nanotubes in water. Environ. Sci. Technol. 48, 11330–11336.

Kalyanaraman, B., Cheng, G., Hardy, M., Ouari, O., Bennett, B., Zielonka, J., 2018. Teaching the basics of reactive oxygen species and their relevance to cancer biology: mitochondrial reactive oxygen species detection, redox signaling, and targeted therapies. Redox Biol. 15, 347–362.

Kang, Y., Liu, J., Wu, J., Yin, Q., Liang, H., Chen, A., Shao, L., 2017. Graphene oxide and reduced graphene oxide induced neural pheochromocytoma-derived PC12 cell lines apoptosis and cell cycle alterations via the ERK signaling pathways. Int J. Nanomed. 12, 5501–5510.

Kang, Y., Liu, J., Yin, S., Jiang, Y., Feng, X., Wu, J., Zhang, Y., Chen, A., Zhang, Y., Shao, L., 2020. Oxidation of reduced graphene oxide via cellular redox signaling modulates actin-mediated neurotransmission. ACS Nano 14, 3059–3074.

Koh, W.L., Tham, P.H., Yu, H., Leo, H.L., Yong, K.J., 2016. Aggregation and protein corona formation on gold nanoparticles affect viability and liver functions of primary rat hepatocytes. Nanomedicine 11, 2275–2287.

Kovalevich, J., Langford, D., 2013. Considerations for the use of SH-SY5Y neuroblastoma cells in neurobiology. Methods Mol. Biol. 1078, 9–21.

Kunovac, A., Hathaway, Q.A., Pinti, M.V., Goldsmith, W.T., Durr, A.J., Fink, G.K., Nurkiewicz, T.R., Hollander, J.M., 2019. ROS promote epigenetic remodeling and cardiac dysfunction in offspring following maternal engineered nanomaterial (ENM) exposure. Part. Fibre Toxicol. 16, 24.

Li, H., Chen, J., Fan, H., Cai, R., Gao, X., Meng, D., Ji, Y., Chen, C., Wang, L., Wu, X., 2020. Initiation of protective autophagy in hepatocytes by gold nanorod core/silver shell nanostructures. Nanoscale 12, 6429–6437.

Li, L., Sha, Z., Wang, Y., Yang, D., Li, J., Duan, Z., Wang, H., Li, Y., 2019. Pre-treatment with a combination of Shenmai and Danshen injection protects cardiomyocytes against hypoxia/reoxygenation- and H2O2-induced injury by inhibiting mitochondrial permeability transition pore opening. Exp. Ther. Med. 17 (6), 4643–4652.

Li, R., Mansukhani, N.D., Guiney, L.M., Ji, Z., Zhao, Y., Chang, C.H., French, C.T., Miller, J.F., Hersam, M.C., Nel, A.E., Xia, T., 2016. Identification and optimization of carbon radicals on hydrated graphene oxide for ubiquitous antibacterial coatings. ACS Nano 10, 10966–10980.

Li, R., Guiney, L.M., Chang, C.H., Mansukhani, N.D., Ji, Z., Wang, X., Liao, Y.P., Jiang, W., Sun, B., Hersam, M.C., Nel, A.E., Xia, T., 2018. Surface oxidation of graphene oxide determines membrane damage, lipid peroxidation, and cytotoxicity in macrophages in a pulmonary toxicity model. ACS Nano 12, 1390–1402.

Liang, Y., Dong, B., Pang, N., Hu, J., 2019. ROS generation and DNA damage contribute to abamectin-induced cytotoxicity in mouse macrophage cells. Chemosphere 234, 328–337.

Liu, L., Zhu, C., Fan, M., Chen, C., Huang, Y., Hao, Q., Yang, J., Wang, H., Sun, D., 2015. Oxidation and degradation of graphitic materials by naphthalene-degrading bacteria. Nanoscale 7, 13619–13628.

Liu, M., Huang, C., Jia, Z., Zhao, Z., Xiao, X., Wang, A., Li, P., Guan, X., Zhou, G., Fan, Y., 2020. Promotion of neuronal guidance growth by aminated graphene oxide via Netrin-1/deleted in colorectal cancer signaling. ACS Chem. Neurosci. 11, 604–614.
Liu, S., Zeng, T.H., Hofmann, M., Burcombe, E., Wei, J., Jiang, R., Kong, J., Chen, Y., 2011. Antibacterial activity of graphite, graphite oxide, graphene oxide, and reduced graphene oxide: membrane and oxidative stress. ACS Nano 5, 6971–6980.
Lu, C.J., Jiang, X.F., Junaid, M., Ma, Y.B., Jia, P.P., Wang, H.B., Pei, D.S., 2017. Graphene oxide nanosheets induce DNA damage and activate the base excision repair (BER) signaling pathway both in vitro and in vivo. Chemosphere 184, 795–805.
Ma, J., Liu, R., Wang, X., Liu, Q., Chen, Y., Valle, R.P., Zuo, Y.Y., Xia, T., Liu, S., 2015. Crucial role of lateral size for graphene oxide in activating macrophages and stimulating pro-inflammatory responses in cells and animals. ACS Nano 9, 10498–10515.
Ma, M.W., Wang, J., Dhandapani, K.M., Wang, R., Brann, D.W., 2018. NADPH oxidases in traumatic brain injury – promising therapeutic targets? Redox Biol. 16, 285–293.
Maktedar, S.S., Avashthi, G., Singh, M., 2017. Ultrasound assisted simultaneous reduction and direct functionalization of graphene oxide with thermal and cytotoxicity profile. Ultrason. Sonochem. 34, 856–864.
Manshian, B.B., Pokhrel, S., Madler, L., Soenen, S.J., 2018. The impact of nanoparticle-driven lysosomal alkalinization on cellular functionality. J. Nanobiotechnol. 16, 85.
Mao, J., Guo, R., Yan, L.T., 2014. Simulation and analysis of cellular internalization pathways and membrane perturbation for graphene nanosheets. Biomaterials 35, 6069–6077.
Martner, A., Aydin, E., Hellstrand, K., 2019. NOX2 in autoimmunity, tumor growth and metastasis. J. Pathol. 247, 151–154.
Mauvezin, C., Neufeld, T.P., 2015. Bafilomycin A1 disrupts autophagic flux by inhibiting both V-ATPase-dependent acidification and Ca-P60A/SERCA-dependent autophagosome-lysosome fusion. Autophagy 11, 1437–1438.
Mindell, J.A., 2012. Lysosomal acidification mechanisms. Annu. Rev. Physiol. 74, 69–86.
Mohammadinejad, R., Moosavi, M.A., Tavakol, S., Vardar, D.Ö., Hosseini, A., Rahmati, M., Dini, L., Hussain, S., Mandegary, A., Klionsky, D.J., 2019. Necrotic, apoptotic and autophagic cell fates triggered by nanoparticles. Autophagy 15, 4–33.
Niu, Q.F., Wang, Q.L., Tong, Z.X., Tong, L., Tong, X.J., 2019. Adsorptive properties of graphene oxide on vitamin B12 and their effect on the promotion of peripheral nerve regeneration. Neurol. Res. 41, 282–288.
Nwadike, C., Williamson, L.E., Gallagher, L.E., Guan, J.L., Chan, E., 2018. AMPK inhibits ULK1-dependent autophagosome formation and lysosomal acidification via distinct mechanisms. Mol. Cell. Biol. 38.
Park, E.J., Lee, G.H., Han, B.S., Lee, B.S., Lee, S., Cho, M.H., Kim, J.H., Kim, D.W., 2015. Toxic response of graphene nanoplatelets in vivo and in vitro. Arch. Toxicol. 89, 1557–1568.
Pattammattel, A., Pande, P., Kuttappan, D., Puglia, M., Basu, A.K., Amalaradjou, M.A., Kumar, C.V., 2017. Controlling the graphene-bio interface: dispersions in animal sera for enhanced stability and reduced toxicity. Langmuir 33, 14184–14194.
Perez-Arizti, J.A., Ventura-Gallegos, J.L., Galvan, J.R., Ramos-Godinez, M., Colin-Val, Z., Lopez-Marure, R., 2020. Titanium dioxide nanoparticles promote oxidative stress, autophagy and reduce NLRP3 in primary rat astrocytes. Chem. Biol. Interact. 317, 108966.
Russier, J., Treossi, E., Scarsi, A., Perrozzi, F., Dumortier, H., Ottaviano, L., Meneghetti, M., Palermo, V., Bianco, A., 2013. Evidencing the mask effect of graphene oxide: a comparative study on primary human and murine phagocytic cells. Nanoscale 5, 11234–11247.
Sasidharan, A., Panchakarla, L.S., Sadanandan, A.R., Ashokan, A., Chandran, P., Girish, C.M., Menon, D., Nair, S.V., Rao, C.N., Koyakutty, M., 2012. Hemocompatibility and macrophage response of pristine and functionalized graphene. Small 8, 1251–1263.
Satapathy, M.K., Manga, Y.B., Ostrikov, K.K., Chiang, W.H., Pandey, A., R, L., Nyambat, B., Chuang, E.Y., Chen, C.H., 2020. Microplasma cross-linked graphene oxide-gelatin hydrogel for cartilage reconstructive surgery. ACS Appl. Mater. Interfaces 12, 86–95.
Shen, H., Lin, H., Sun, A.X., Song, S., Wang, B., Yang, Y., Dai, J., Tuan, R.S., 2020. Acceleration of chondrogenic differentiation of human mesenchymal stem cells by sustained growth factor release in 3D graphene oxide incorporated hydrogels. Acta Biomater. 105, 44–55.
Shen, J., Yang, D., Zhou, X., Wang, Y., Tang, S., Yin, H., Wang, J., Chen, R., Chen, J., 2019. Role of autophagy in zinc oxide nanoparticles-induced apoptosis of mouse LEYDIG cells. Int. J. Mol. Sci. 20.
Simonet, S., Rodriguez-Lafrasse, C., Beal, D., Gerbaud, S., Malesys, C., Tillement, O., Lux, F., Fayyad-Kazan, H., Rachidi, W., Ardail, D., 2020. Gadolinium-based nanoparticles can overcome the radioresistance of head and neck squamous cell carcinoma through the induction of autophagy. J. Biomed. Nanotechnol. 16, 111–124.
Singh, S.K., Singh, M.K., Kulkarni, P.P., Sonkar, V.K., Gracio, J.J., Dash, D., 2012. Amine-modified graphene: thrombo-protective safer alternative to graphene oxide for biomedical applications. ACS Nano 6, 2731–2740.
Soenen, S.J., Parak, W.J., Rejman, J., Manshian, B., 2015. Intracellular stability of inorganic nanoparticles: effects on cytotoxicity, particle functionality, and biomedical applications. Chem. Rev. 115, 2109–2135.
Stefanatos, R., Sanz, A., 2018. The role of mitochondrial ROS in the aging brain. FEBS Lett. 592, 743–758.
Sun, Y., Zheng, Y., Wang, C., Liu, Y., 2018. Glutathione depletion induces ferroptosis, autophagy, and premature cell senescence in retinal pigment epithelial cells. Cell Death Dis. 9 (7), 753.
Tsutsumi, K., Sasase, T., 2019. Cellular calcification induced by inorganic polyphosphate involves ATP depletion and opening of the mitochondrial permeability transition pore (mPTP). FEBS Open Bio 9 (9), 1617–1622.
Valko, M., Jomova, K., Rhodes, C.J., Kuca, K., Musilek, K., 2016. Redox- and non-redox-metal-induced formation of free radicals and their role in human disease. Arch. Toxicol. 90, 1–37.
Wang, W., Zhu, M., Xu, Z., Li, W., Dong, X., Chen, Y., Lin, B., Li, M., 2019. Ropivacaine promotes apoptosis of hepatocellular carcinoma cells through damaging mitochondria and activating caspase-3 activity. Biol. Res. 52 (1), 36.
Wu, N.N., Zhang, Y., Ren, J., 2019. Mitophagy, mitochondrial dynamics, and homeostasis in cardiovascular aging. Oxid. Med. Cell. Longev. 2019, 9825061.
Xiao, D., He, H., Huang, W., Oo, T.L., Wang, A., He, L.F., 2018. Analysis of mitochondrial markers of programmed cell death. Methods Mol. Biol. 1743, 65–71.
Xiaoli, F., Junrong, W., Xuan, L., Yanli, Z., Limin, W., Jia, L., Longquan, S., 2017. Prenatal exposure to nanosized zinc oxide in rats: neurotoxicity and postnatal impaired learning and memory ability. Nanomedicine 12, 777–795.
Xiaoli, F., Qiyue, C., Weihong, G., Yaqing, Z., Chen, H., Junrong, W., Longquan, S., 2020. Toxicology data of graphene-family nanomaterials: an update. Arch. Toxicol. 94, 1915–1939.
Xicoy, H., Wieringa, B., Martens, G.J., 2017. The SH-SY5Y cell line in Parkinson's disease research: a systematic review. Mol. Neurodegener. 12 (1), 10. Jan 24.
Xu, M., Zhu, J., Wang, F., Xiong, Y., Wu, Y., Wang, Q., Weng, J., Zhang, Z., Chen, W., Liu, S., 2016. Improved in vitro and in vivo biocompatibility of graphene oxide through surface modification: poly(acrylic acid)-functionalization is superior to PEGylation. ACS Nano 10, 3267–3281.
Yamashita, S.I., Kanki, T., 2017. How autophagy eats large mitochondria: autophagosome formation coupled with mitochondrial fragmentation. Autophagy 13, 980–981.
Yang, Q., Wang, Y., Yang, Q., Gao, Y., Duan, X., Fu, Q., Chu, C., Pan, X., Cui, X., Sun, Y., 2017. Cuprous oxide nanoparticles trigger ER stress-induced apoptosis by regulating copper trafficking and overcoming resistance to sunitinib therapy in renal cancer. Biomaterials 146, 72–85.
Yang, Y., Karakhanova, S., Hartwig, W., D'Haese, J.G., Philippov, P.P., Werner, J., Bazhin, A.V., 2016. Mitochondria and mitochondrial ROS in cancer: novel targets for anticancer therapy. J. Cell. Physiol. 231, 2570–2581.
Yao, J., Wang, H., Chen, M., Yang, M., 2019. Recent advances in graphene-based nanomaterials: properties, toxicity and applications in chemistry, biology and medicine. Mikrochim. Acta 186, 395.
Zhang, B., Wei, P., Zhou, Z., Wei, T., 2016. Interactions of graphene with mammalian cells: molecular mechanisms and biomedical insights. Adv. Drug Deliv. Rev. 105, 145–162.
Zhang, F., You, X., Zhu, T., Gao, S., Wang, Y., Wang, R., Yu, H., Qian, B., 2020. Silica nanoparticles enhance germ cell apoptosis by inducing reactive oxygen species (ROS) formation in Caenorhabditis elegans. J. Toxicol. Sci. 45, 117–129.
Zhang, R., Li, G., Zhang, Q., Tang, Q., Huang, J., Hu, C., Liu, Y., Wang, Q., Liu, W., Gao, N., Zhou, S., 2018. Hirsutine induces mPTP-dependent apoptosis through ROCK1/PTEN/PI3K/GSK3β pathway in human lung cancer cells. Cell Death Dis. 9, 598.
Zhang, X., Yin, H., Li, Z., Zhang, T., Yang, Z., 2016. Nano-TiO2 induces autophagy to protect against cell death through antioxidative mechanism in podocytes. Cell Biol. Toxicol. 32, 513–527.
Zhang, X., Cheng, X., Yu, L., Yang, J., Calvo, R., Patnaik, S., Hu, X., Gao, Q., Yang, M., Lawas, M., Delling, M., Marugan, J., Ferrer, M., Xu, H., 2016. MCOLN1 is a ROS sensor in lysosomes that regulates autophagy. Nat. Commun. 7, 12109.
Zhang, X., Guo, X., Kang, X., Yang, H., Guo, W., Guan, L., Wu, H., Du, L., 2020. Surface functionalization of pegylated gold nanoparticles with antioxidants suppresses nanoparticle-induced oxidative stress and neurotoxicity. Chem. Res. Toxicol. 33, 1195–1205.
Zhao, X., Wei, S., Li, Z., Lin, C., Zhu, Z., Sun, D., Bai, R., Qian, J., Gao, X., Chen, G., Xu, Z., 2019. Autophagic flux blockage in alveolar epithelial cells is essential in silica nanoparticle-induced pulmonary fibrosis. Cell Death Dis. 10 (2), 127.
Zhao, Y., Jafvert, C.T., 2015. Environmental photochemistry of single layered graphene oxide in water. Environ. Sci. 2, 136–142.